

Berkeley Supernova Ia Program III: Spectra Near Maximum Brightness Improve the Accuracy of Derived Distances to Type Ia Supernovae

Jeffrey M. Silverman,^{1,2*} Mohan Ganeshalingam,¹ Weidong Li,^{1†}
 Alexei V. Filippenko¹

¹*Department of Astronomy, University of California, Berkeley, CA 94720-3411, USA*

²*Marc J. Staley Fellow*

[†]*Deceased 12 December 2011*

Accepted . Received ; in original form

ABSTRACT

In this third paper in a series we compare spectral feature measurements to photometric properties of 108 low-redshift ($z < 0.1$, $< z > \approx 0.023$) Type Ia supernovae (SNe Ia) for which we have optical spectra within 5 d of maximum brightness. The spectral data were obtained from 1989 through the end of 2008 as part of the Berkeley SN Ia Program (BSNIP) and are presented in BSNIP I (Silverman et al. 2012), and the photometric data come mainly from the Lick Observatory Supernova Search (LOSS) and are published by Ganeshalingam et al. (2010). The spectral measurements are presented and discussed in BSNIP II (Silverman, Kong & Filippenko 2012), and the light-curve fits and photometric parameters can be found in Ganeshalingam et al. (in preparation). A variety of previously proposed correlations between spectral and photometric parameters are investigated using the large and self-consistent BSNIP dataset. We find *the pseudo-equivalent width (pEW) of the Si II $\lambda 4000$ line to be a good indicator of light-curve width, and the pEWs of the Mg II and Fe II complexes are relatively good proxies for SN colour.* We also employ a combination of light-curve parameters (specifically the SALT2 stretch and colour parameters x_1 and c , respectively) and spectral measurements to calculate distance moduli. The residuals from these models are then compared to the standard model which uses only light-curve stretch and colour. Our investigations show that *a distance model that uses x_1 , c , and the velocity of the Si II $\lambda 6355$ feature does not lead to a decrease in the Hubble residuals.* We also find that *distance models with flux ratios alone or in conjunction with light-curve information rarely perform better than the standard (x_1, c) model.* However, *when adopting a distance model which combines the ratio of fluxes near ~ 3750 Å and ~ 4550 Å with both x_1 and c , the Hubble residuals are decreased by ~ 10 per cent, which is found to be significant at about the 2σ level. The weighted root-mean-square of the residuals using this model is 0.130 ± 0.017 mag (as compared with 0.144 ± 0.019 mag when using the same sample with the standard model).* This Hubble diagram fit has one of the smallest scatters ever published and at the highest significance ever seen in such a study. Finally, these results are discussed with regard to how they can improve the cosmological accuracy of future, large-scale SN Ia surveys.

Key words: methods: data analysis – supernovae: general – cosmology: observations – distance scale

1 INTRODUCTION

Type Ia supernovae (SNe Ia) have been used in the recent past to discover the accelerating expansion of the Universe

(Riess et al. 1998; Perlmutter et al. 1999), as well as to measure cosmological parameters with increasing accuracy and precision (e.g., Astier et al. 2006; Riess et al. 2007; Wood-Vasey et al. 2007; Hicken et al. 2009; Kessler et al. 2009; Amanullah et al. 2010; Sullivan et al. 2011; Suzuki et al. 2012). In the most general terms, thermonuclear ex-

* E-mail: JSilverman@astro.berkeley.edu

plosions of carbon/oxygen (C/O) white dwarfs (WDs) are thought to give rise to SNe Ia (e.g., Hoyle & Fowler 1960; Colgate & McKee 1969; Nomoto et al. 1984; see Hillebrandt & Niemeyer 2000 for a review). However, after decades of observations and theoretical work, a detailed understanding of both the SN progenitors and explosion mechanisms is still missing. In addition, there is very little known about how differences in the initial conditions in SNe Ia give rise to the measured range of observables. A large, self-consistent dataset is needed in order to solve these problems.

The ability to do precision cosmology using SNe Ia requires that one is able to calibrate or standardise their luminosity. Phillips (1993) showed a tight correlation between light-curve decline rate and luminosity at peak brightness for the majority of SNe Ia, the so-called ‘‘Phillips relation.’’ However, the addition of spectral observations to the light-curve data complicates the picture far beyond the simple assumption underlying the Phillips relation. Many comparisons of spectral and photometric data of low-redshift SNe Ia have been performed in the past (e.g., Nugent et al. 1995; Benetti et al. 2005; Bongard et al. 2006; Hachinger et al. 2006; Arsenijevic et al. 2008; Walker et al. 2011; Nordin et al. 2011b; Blondin et al. 2011; Chotard et al. 2011). In addition, there has been similar work with SNe Ia at higher redshifts (e.g., Blondin et al. 2006; Altavilla et al. 2009; Nordin et al. 2011b; Walker et al. 2011). These studies were often aimed at finding a ‘‘second parameter’’ in SN Ia spectral or photometric data which would increase the accuracy of their distance measurements.

Most of these previous studies utilised relatively small and heterogeneous datasets. The data studied here, in contrast, were self-consistently observed and reduced, and constitute one of the largest datasets to be analysed in this manner. Low-redshift ($z \leq 0.1$, $< z \approx 0.023$) optical SN Ia spectra from the Berkeley Supernova Ia Program (BSNIP; Silverman et al. 2012) are used along with complementary photometric data, largely from Ganeshalingam et al. (2010). The spectral features have been accurately and robustly measured (BSNIP II; Silverman, Kong & Filippenko 2012), and the light curves have been fit using a variety of methods (Ganeshalingam et al., in preparation).

We summarise both the spectral and photometric datasets used for this analysis in Section 2, and we describe our procedure for measuring spectral features, fitting light curves, and producing Hubble diagrams in Section 3. How these measured values correlate with each other and with previously determined classifications is presented in Section 4, along with our Hubble diagram results using various models for the distances to SNe Ia. We present our conclusions in Section 5, where the main results of our analysis are summarised and the most accurate and useful spectral indicators are discussed. Other, future BSNIP papers will expand on the analysis performed here with the addition of host-galaxy properties and late-time SN spectra.

2 DATASET

2.1 Spectral Data

The same SN Ia spectral data are analysed in the current study as were used in BSNIP II. The spectra are all origi-

nally published in BSNIP I. Most of the spectra were obtained using the Shane 3 m telescope at Lick Observatory with the Kast double spectrograph (Miller & Stone 1993), and the typical wavelength coverage is 3300–10,400 Å with resolutions of ~ 11 Å and ~ 6 Å on the red and blue sides (crossover wavelength ~ 5500 Å), respectively. See BSNIP I For more information regarding the observations and data reduction.

In BSNIP II, we required that a spectrum be within 20 d (rest frame) of maximum brightness and we *a priori* ignored the extremely peculiar SN 2000cx (e.g., Li et al. 2001), SN 2002cx (e.g., Li et al. 2003; Jha et al. 2006), SN 2005hk (e.g., Chornock et al. 2006; Phillips et al. 2007), and SN 2008ha (e.g., Foley et al. 2009; Valenti et al. 2009). BSNIP II contains 432 spectra of 261 SNe Ia with a ‘‘good’’ fit for at least one spectral feature. However, only a subset of these data are used in the current study since not all of them have reliable photometric observations and we are currently only considering spectra within 5 d of maximum brightness. It was shown in BSNIP II that the spectral measurements do not evolve significantly during these epochs. For the 11 SNe Ia that had more than one spectrum within 5 d of maximum brightness and photometric information, we only use the spectrum closest to the date of maximum in the current analysis.

For our investigation using arbitrary ratios of fluxes (see Section 4.10) we also use spectra within 5 d of maximum brightness, even though previous studies only investigated spectra within 2.5 d of maximum (Bailey et al. 2009; Blondin et al. 2011). When we employ spectra only in this narrower age range, our sample size for the flux-ratio analysis decreases from 62 to 38 objects. While our overall results are mostly unchanged when considering only spectra within 2.5 d of maximum brightness, their significance is weakened due to the smaller number of objects used. Adopting a larger age range than within 5 d of maximum increases the sample size only moderately and introduces much larger scatter in spectral measurements (see BSNIP II).

2.2 Photometric Data

A majority of the SNe in our spectral sample were discovered as part of the Lick Observatory Supernova Search (LOSS). LOSS is a transient survey utilising the 0.76-m Katzman Automatic Imaging Telescope (KAIT) at Lick Observatory (Li et al. 2000; Filippenko et al. 2001; see also Filippenko, Li, & Treffers, in preparation). KAIT is a robotic telescope that monitors a sample of $\sim 15,000$ galaxies in the nearby Universe (redshift $z < 0.05$) with the goal of finding transients within days of explosion. Fields are imaged every 3–10 d and compared to archived template images, after which potential new transients are flagged. These images are examined by human image checkers and the best candidates are re-observed the following night. Candidates that are present on two consecutive nights are reported to the community using the International Astronomical Union Circulars (IAUCs) and the Central Bureau of Electronic Telegrams (CBETs). The statistical power of the LOSS sample is well demonstrated by the series of papers deriving nearby SN rates (Leaman et al. 2011; Li et al. 2011a,b).

In addition to the SN search, KAIT monitors active SNe of all types in broad-band *BVRI* filters. The first data

release of *BVRI* light curves for 165 SNe Ia along with details about the reduction procedure have been published by Ganeshalingam et al. (2010). In summary, point-spread function (PSF) fitting photometry is performed on images from which the host galaxy has been subtracted using templates obtained > 1 yr after explosion. Photometry is transformed to the Landolt system (Landolt 1983, 1992) using averaged colour terms determined over many photometric nights. Calibrations for each SN field are obtained on photometric nights with an average of 5 calibrations per field.

We also include SN Ia light curves obtained from the literature to maximise the overlap between our photometric and spectroscopic samples. We include 29 objects from the Calán-Tololo sample (Hamuy et al. 1996), 22 objects from the CfA1 sample (Riess et al. 1999), 44 objects from CfA2 (Jha et al. 2006), and 185 objects from CfA3 (Hicken et al. 2009). In instances where we have data for the same SN from multiple samples, we use the light curve that is most densely sampled and best captures the light-curve evolution. We also include light curves for SNe 1999aw (Strolger et al. 2002), 1999ee, 2000bh, 2000ca, 2001ba (Krisciunas et al. 2004a), 2001bt, 2001cn, and 2001cz (Krisciunas et al. 2004b). Our final photometry sample consists of 335 multi-colour light curves, though we note that not all the objects in this sample have corresponding spectroscopy.

Of the data within 5 d of maximum brightness investigated in BSNIP II, 115 SNe have light-curve width or colour information and are included in the present study. The redshift range spanned by this sample is $0 < z < 0.1$. A complete list of these SNe Ia, their ages, spectral classifications, and spectral feature measurements can be found in BSNIP II. The photometric parameters of these objects are presented by Ganeshalingam et al. (in preparation).

3 MEASUREMENT PROCEDURES

3.1 Spectral Measurements

The algorithm used to measure each of nine spectral features and the features themselves are described in detail in BSNIP II. Here we give a brief summary of the procedure.

Each spectrum has its host-galaxy recession velocity removed and is corrected for Galactic reddening (according to the values presented in Table 1 of BSNIP I), and it is smoothed using a Savitzky-Golay smoothing filter (Savitzky & Golay 1964). If the signal-to-noise ratio (S/N) is larger than 6.5 pixel^{-1} over the entire spectral range, we attempt to define a pseudo-continuum for each spectral feature. This is done by determining where the local slope changes sign on either side of the feature's minimum. Quadratic functions are fit to each of these endpoints and the peaks of the parabolas (assuming that they are both concave downward) are used as the endpoints of the feature; they are then connected with a line to define the pseudo-continuum. We record the flux at the blue and red endpoints of the feature (F_b and F_r , respectively) as well as the pseudo-equivalent width (pEW; e.g., Garavini et al. 2007).

Once a pseudo-continuum is calculated, a cubic spline is fit to the smoothed data between the endpoints of the

spectral feature.¹ From the wavelength at which the spline fit reaches its minimum (λ_{\min}) the expansion velocity (v) is calculated. The flux is then normalised to the pseudo-continuum, and the relative depth of the feature (a) and its full-width at half-maximum (FWHM) are computed. Finally, every spectral feature in each spectrum is visually inspected by more than one person and removed from the study if the spline fit and/or pseudo-continuum do not accurately reflect the spectral feature.

3.2 Light-Curve Fitting

A variety of methods have been developed to measure the photometric properties of SN Ia light curves. Here, we describe three different light-curve fitting methods adopted in this paper to characterise the SN Ia light curves. While the light-curve parameters derived from each of these methods are degenerate to some extent, it is useful to perform all three fitting techniques for the purpose of comparing our results to previous results in the literature. There are also cases, for certain spectroscopic subtypes, where one method is superior to the other two.

3.2.1 Template and Polynomial Fitting

Our most direct measurement of light-curve properties makes use of the template-fitting routine introduced by Prieto et al. (2006). For a given photometric bandpass, a set of template light curves is used to construct models which match the light-curve data. The model light curves are linear combinations of the template light curves using the weighting scheme described by Ganeshalingam et al. (2010). A χ^2 -minimisation fitting routine is used to determine the combination of templates that best fits the data. For band X , we measure the date of maximum brightness, the apparent peak magnitude (m_X), and the light-curve width parametrised as the difference in magnitudes between maximum and fifteen days past maximum, $\Delta m_{15}(X)$. We independently fit the B - and V -band light curves for the SNe in our sample.

In instances where we have a well-sampled light curve, but cannot achieve an acceptable fit with our template-fitting routine, we fit the data with a fourth-order polynomial.

For both the template- and polynomial-fitting routines, we use a Monte Carlo routine to measure the uncertainty in our derived parameters. We simulate realisations of our dataset by randomly perturbing each data point by its 1σ photometric error assuming a Gaussian distribution centred at 0 mag. We fit the dataset realisation with our fitting routine and measure light-curve properties for that simulation. We estimate the uncertainty in our derived parameters to be the standard deviation of 50 dataset realisations.

¹ No attempt is made to fit any of the Mg II or Fe II features in this manner; these complexes consist of so many blended spectral lines that it is unclear which reference wavelength to use when attempting to define an expansion velocity.

3.2.2 MLCS2k2

The Multi-colour Light Curve Shape (MLCS) distance-fitting software was first introduced by Riess et al. (1996) to simultaneously fit all light-curve data for a given SN Ia to produce a distance estimate. This method relies on the observation that more luminous SNe Ia have broader light curves (Phillips 1993) and also have bluer colours during the photospheric phase. MLCS parametrises light-curve width using the parameter Δ , which measures the difference in absolute magnitude of the SN with reference to a fiducial SN Ia. MLCS attempts to disentangle intrinsic colour variations from host-galaxy effects to also produce an estimate for host-galaxy extinction, A_V . MLCS2k2.v006 (referred to as simply MLCS2k2 for the rest of this work; Jha et al. 2007) is the most current publicly available implementation of this fitting routine. In comparison to the original version, it has an expanded set of training templates and improvements in the treatment of host reddening and K -corrections.

For our analysis with MLCS2k2, we use the galactic line-of-sight prior which models the distribution of host-galaxy extinction values as a decaying exponential with a peak value of 0 mag (Hatano et al. 1998). We also set the host-galaxy $R_V = 1.7$ based on the cosmological analysis of Hicken et al. (2009). Their analysis found that a lower host-galaxy R_V reduced the scatter in the Hubble diagram compared to a more typical Galactic value of $R_V = 3.1$. A fit using MLCS2k2 is considered reliable (and thus its parameters are used in the current analysis) only when the reduced $\chi^2 \leq 1.6$.

3.2.3 SALT2

Spectral Adaptive Light-curve Template (SALT) was first developed by the SuperNova Legacy Survey (SNLS) (Guy et al. 2005). Calculating distances with SALT is a two-step process. SALT first measures light-curve parameters that are expected to correlate with the intrinsic brightness of individual SNe (i.e., light-curve width and colour). Then a model for the corrected apparent magnitude of a SN, $m_{B,\text{corr}}$, is adopted which applies linear corrections for the light-curve width and colour to the measured apparent magnitude, m_B . Thus, the corrected apparent magnitude has the form

$$m_{B,\text{corr}} = m_B + \alpha \times (\text{light-curve width}) - \beta \times (\text{colour}). \quad (1)$$

The constants α and β are found by minimising χ^2 using distance estimates from a large sample of SNe Ia compared to a cosmological model (see Section 3.3 for more details).

SALT2 is an updated version of SALT with an expanded training set of light-curve templates and is the version implemented here. SALT2 is trained on light curves and spectra from low- z SNe compiled from the literature and high- z SNe from the first two years of the SNLS (Guy et al. 2007). SALT2 measures a parametrisation of the light-curve width (x_1), the SN colour (c), and the apparent B -band magnitude at maximum light (m_B).

In fitting our light curves, we exclude I -band data, which are not included in the SALT2 template set. We also exclude subluminous SNe Ia, often of the spectral subclass of SN 1991bg-like objects (e.g., Filippenko et al. 1992b; Leibundgut et al. 1993), since SALT2 was not developed to fit this particular subtype. This is achieved by using only

SNe Ia with $-3 \leq x_1 \leq 2$ (as in Blondin et al. 2011). Finally, the results of SALT2 fits are utilised here only when the reduced $\chi^2 < 2$.

3.3 Hubble Diagrams

In this section we present the methodology used to standardise SNe Ia for cosmological application. We use a model that applies linear corrections for light-curve width and colour. The width of a light curve correlates with the intrinsic luminosity in the sense that SNe with broader light curves are also more luminous. This correlation has been well established (Phillips 1993). The colour parameter combines the effects of intrinsic colour variations and host-galaxy reddening. We use the SALT2 parameters x_1 and c as the parametrisations of light-curve width and SN colour, respectively. We will also generalise this approach to allow for linear corrections using spectroscopic parameters.

The distance modulus for each SN can be estimated from its redshift by $\mu(z) = 25 + 5 \log_{10}[D_L(z)]$, where D_L is the luminosity distance expressed in units of Mpc. The distance modulus including linear corrections for light-curve width and colour can be expressed as

$$\mu_{\text{SN}} = m_B - M + \alpha x_1 - \beta c. \quad (2)$$

The variables α , β , and M (the fiducial absolute magnitude of a SN Ia) are determined by using a custom version of `cosfitter` (A. Conley, 2011, private communication) based on the `Minuit` minimisation package (James & Roos 1975). The software minimises the function

$$\chi^2 = \sum_{s=1}^N \frac{(\mu(z_s) - \mu_{\text{SN},s})^2}{\sigma_{\text{m},s}^2 + \sigma_{\text{pec},s}^2 + \sigma_{\text{int}}^2}, \quad (3)$$

where $\mu(z)$ is the distance modulus of the galaxy in the cosmic microwave background (CMB) rest-frame redshift z , σ_{m} is the measurement error in light-curve properties accounting for covariances between measured parameters, σ_{pec} is the uncertainty due to deviations from Hubble's law induced by gravitational interactions from neighbouring galaxies, and σ_{int} is a constant intrinsic scatter added to each SN to achieve a reduced $\chi^2 \approx 1$. We adopt 300 km s^{-1} as the peculiar velocity for each SN. The intrinsic scatter, σ_{int} , can be considered as the uncertainty associated with a model that attempts to standardise SNe using the parameters x_1 and c .

Only objects with $z_{\text{helio}} > 0.01$ are used in the Hubble diagrams in order to avoid including SNe with motions dominated by peculiar velocities. We also adopt the same Hubble diagram colour cut as Blondin et al. (2011), who exclude objects with $c > 0.50$. Finally, as mentioned above, all analysis using SALT2 fits is restricted to objects with a reduced $\chi^2 < 2$.

In this work we consider nearby SNe (median $z_{\text{CMB}} \approx 0.021$) and are not attempting to find a best-fitting cosmology. A goal of this study is to combine photometric and spectroscopic properties such that SNe Ia become more accurate standardisable candles. We also aim to quantify the amount of improvement when using a variety of observed measurements. To that end, we adopt the standard Λ CDM cosmology with $\Omega_{\text{m}} = 0.27$, $\Omega_{\Lambda} = 0.73$, and $w = -1$ when calculating $\mu(z)$.

3.3.1 Models for Predicting SN Ia Distances

Here we describe the generalisation of our calculation of the distance modulus for each SN to allow for linear corrections using measured spectral parameters (such as velocity and pEW; see Sections 4.2 and 4.4) or the ratios of pEWs and fluxes (such as $\mathfrak{R}(\text{Si II})$ and \mathcal{R} ; see Sections 4.5 and 4.10). We consider five models for predicting distances to SNe Ia using combinations of the SALT2 measured light-curve parameters (x_1 and c) and spectral measurements:

$$\mu_{\text{SN}} = m_B - M + \gamma\mathcal{S}, \quad (4)$$

$$\mu_{\text{SN}} = m_B - M + \alpha x_1 + \gamma\mathcal{S}, \quad (5)$$

$$\mu_{\text{SN}} = m_B - M - \beta c + \gamma\mathcal{S}, \quad (6)$$

$$\mu_{\text{SN}} = m_B - M + \alpha x_1 - \beta c + \gamma\mathcal{S}, \quad (7)$$

$$\mu_{\text{SN}} = m_B - M + \alpha x_1 - \beta c. \quad (8)$$

Here, \mathcal{S} represents any spectral measurement: v , pEW, $\mathfrak{R}(\text{Si II})$, \mathcal{R} , etc. The last model included in our study was already mentioned above (Equation 2) and is the model usually adopted in cosmological studies of SNe Ia using only light-curve parameters (e.g., Astier et al. 2006; Kowalski et al. 2008; Hicken et al. 2009; Amanullah et al. 2010). In the following analysis the so-called (x_1, c) model will be the one to which we compare the other cosmological models that include spectral information.

3.3.2 Cross-Validation

Ideally, with a sufficiently large sample, the predictive abilities of a model could be inferred by inspecting the dispersion of the residuals. However, for samples of limited size, the dispersion of the residuals is prone to statistical fluctuations and may not accurately reflect the true predictive nature of the model. Furthermore, for a fixed sample, one can always reduce the dispersion of the residuals by adding more variables to the model. However, it is not clear whether the added variables are actually improving the model itself or simply fitting to the noise inherent in the observables. For analysing the predictive nature of a model, it is useful to perform some form of cross-validation (CV) in which a subset of the entire sample is used to train the model and another subset is used to validate the predictive ability of that model.

Bailey et al. (2009) use a sample of 58 SNe, 28 of which are adopted as a training set to train a model and the other 30 are used as a validation set to assess the predictivity of the model. Using a smaller sample of 26 SNe, Blondin et al. (2011) use a K -fold CV method that allows all of the SNe to be used in the training and validation procedure. For this study, and following Blondin et al. (2011), we adopt the K -fold CV with $K = 10$. We also tested CV with $K = 2, 5$, and 62 and find that our final results are mostly unchanged (however, see Section 4.10.2 for more on our $K = 2$ run). The basics of the procedure are best illuminated by an example, as follows.

Let us begin with a sample of 60 SNe. 10-fold CV starts by randomly dividing the sample into 10 subgroups of 6 SNe each. The first subgroup is set aside; this will be our first validation set. We combine the remaining 9 subgroups and train our model on the 54 other SNe to determine the best-fitting parameters (i.e., α, β, γ , and M). Using the best-fitting pa-

rameters found with the training set, we apply our model to the validation set and calculate the Hubble residual for each of the 6 SNe in our validation set. We repeat this process using the second subgroup as the validation set and the union of the other 9 subgroups as the training set. This process is repeated a total of 10 times (once for each subgroup as a validation set) until we have calculated a residual for every SN in the sample.

3.3.3 Comparing the Models

As in Blondin et al. (2011), the dispersion in each model is estimated using the weighted root-mean-square (WRMS),

$$\text{WRMS}^2 = \frac{\sum_{s=1}^N w_s [\mu(z_s) - \mu_{\text{SN},s}]^2}{\sum_{s=1}^N w_s}, \quad (9)$$

where the weights, w_s , are given by

$$w_s = \sigma_{m,s}^2 + \sigma_{\text{pec},s}^2 + \sigma_{\text{int}}^2. \quad (10)$$

The variance in WRMS is estimated as

$$\text{Var}[\text{WRMS}] = \left[\sum_{s=1}^N w_s \right]^{-1}. \quad (11)$$

The 1σ uncertainty is found by taking the square root of the variance. This is a more appropriate estimator of the dispersion in the model than simply taking the standard deviation in the residuals since we are not guaranteed that the mean residual will be zero (Blondin et al. 2011).

Following Blondin et al. (2011), for each model which uses a spectral measurement (Equations 4–7) we also calculate the intrinsic prediction error (σ_{pred}), the intrinsic correlation ($\rho_{x_1,c}$) of the residuals with residuals using the (x_1, c) model (Equation 8), and the difference ($\Delta_{x_1,c}$) in intrinsic prediction error with respect to the (x_1, c) model. An uncertainty can be computed for $\Delta_{x_1,c}$ (Appendix B of Blondin et al. 2011), and thus the significance of the difference between a given model and the standard (x_1, c) model can also be computed. This parameter is the most direct comparison of how much better (or worse) a model which utilises a spectral measurement is compared to the (x_1, c) model, and how significant the change is. Note that $\Delta_{x_1,c} < 0$ represents an improvement over the (x_1, c) model.

4 ANALYSIS

4.1 Velocity Gradients

Benetti et al. (2005) defined the velocity gradient, $\dot{v} = -\Delta v / \Delta t$, as the “average daily rate of decrease of the expansion velocity” of the Si II $\lambda 6355$ feature and used this parameter to place each of their 26 SNe Ia into one of three categories. The high velocity gradient (HVG) group had the largest velocity gradients ($\dot{v} \gtrsim 70 \text{ km s}^{-1} \text{ d}^{-1}$) and the low velocity gradient (LVG) group had the smallest velocity gradients. The third subclass (FAINT) had the lowest expansion velocities, yet moderately large velocity gradients, and consisted of subluminous SNe Ia with the narrowest light curves ($\Delta m_{15}(B) \gtrsim 1.6 \text{ mag}$).

Even though the BSNIP sample is not well suited to velocity gradient measurements (the average number of spectra per object is ~ 2 , shown in BSNIP I), we are still able to

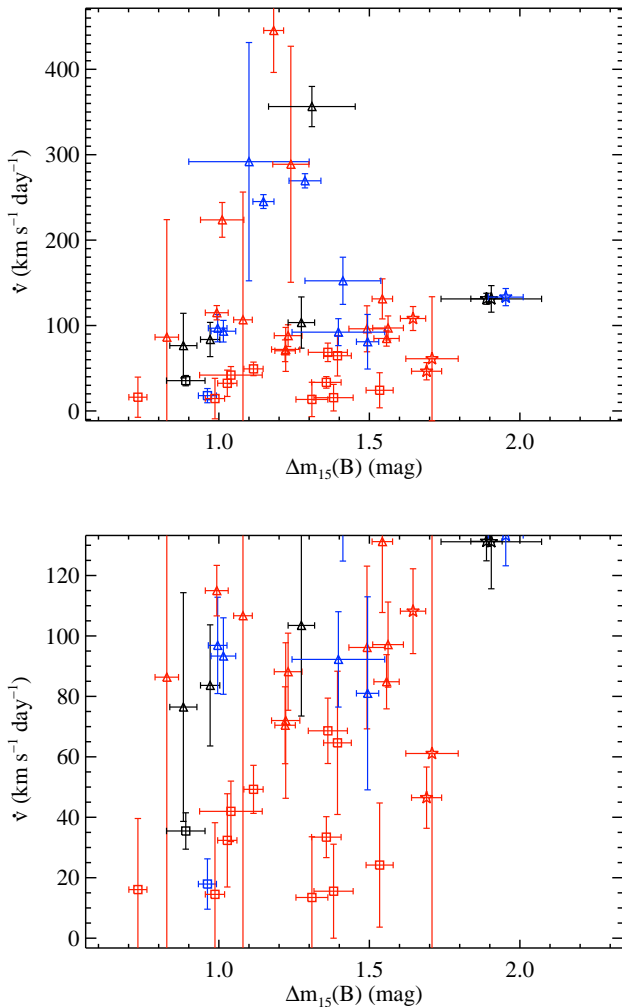


Figure 1. The velocity gradient versus $\Delta m_{15}(B)$ of 44 SNe (*top*) and a close-up view of the low- \dot{v} objects (*bottom*). Blue points are high-velocity (HV) objects, red points are normal-velocity objects, and black points are objects for which we could not determine whether the SN was normal or high velocity (see BSNIP II for further details regarding how HV SNe are defined). Stars are FAINT objects, squares are low velocity gradient (LVG) objects, and triangles are high velocity gradient (HVG) objects (see BSNIP II for further details regarding how these subclasses are defined).

calculate a \dot{v} value for many of our SNe Ia. Figure 1 shows 44 objects and their \dot{v} measurements plotted against their $\Delta m_{15}(B)$ values. The points are colour-coded by their near-maximum Si II $\lambda 6355$ velocity, with red points representing normal-velocity objects and blue points representing high-velocity (HV) objects. These so-called “Wang types” were first presented by Wang et al. (2009), and in BSNIP II we discuss our definition of these subclasses in more detail. The data are also shape-coded by the aforementioned “Benetti types” (FAINT are stars, LVG are squares, and HVG are triangles). The top panel of Figure 1 shows all objects for which a \dot{v} and $\Delta m_{15}(B)$ are measured, while the bottom panel shows a close-up view of the same data such that the axis ranges match those of Figure 3b of Benetti et al. (2005).

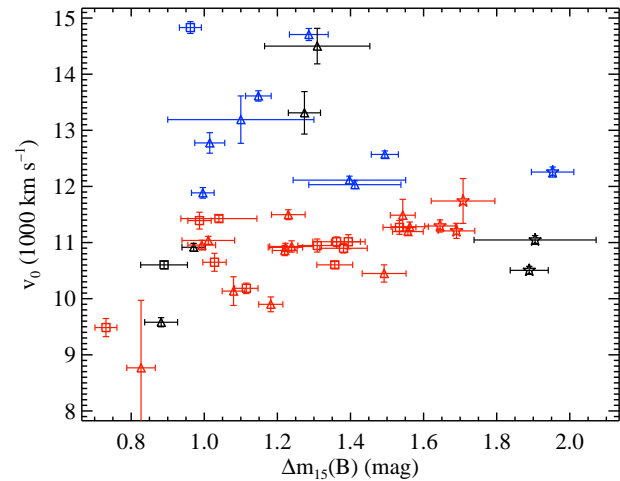


Figure 2. The velocity at maximum brightness of the Si II $\lambda 6355$ feature versus $\Delta m_{15}(B)$ of 44 SNe. Colours and shapes of data points are the same as in Figure 1.

As a result of the definitions of the different subclasses, the FAINT SNe are found to the right in Figure 1 (i.e., large $\Delta m_{15}(B)$ values) and the HVG SNe are found in the upper part of the Figure (i.e., large \dot{v} values), though there is no obvious break between the various classes. As pointed out in BSNIP II and confirmed in Figure 1, the HVG and LVG objects have similar average $\Delta m_{15}(B)$ values and ranges of values.

It was stated by Benetti et al. (2005) that \dot{v} is weakly correlated with $\Delta m_{15}(B)$, though there is no evidence of such a correlation in the BSNIP data. They also claim that there are three distinct families of SNe Ia (LVG, HVG, and FAINT) based partially on their plot of \dot{v} versus $\Delta m_{15}(B)$. With almost 70 per cent more objects, the BSNIP data fill in this parameter space and cast serious doubt on the existence of truly distinct families of SNe Ia based on velocity-gradient measurements (see Table 4 of BSNIP II for the median values of \dot{v} and $\Delta m_{15}(B)$ for each of these three subclasses).

4.2 Expansion Velocities

4.2.1 Velocities at Maximum Brightness

Expansion velocities of SNe Ia are calculated from the minima of various absorption features (see BSNIP II for more information on how this measurement is performed on the data presented here). These velocities have been compared to light-curve width measurements and photometric colours in a variety of ways (e.g., Hachinger et al. 2006; Blondin et al. 2011; Nordin et al. 2011b). As discussed in BSNIP II, Hachinger et al. (2006) interpolate/extrapolate their expansion velocities to the time of maximum brightness (i.e., $t = 0$ d), and v_0 was defined as the expansion velocity of Si II $\lambda 6355$ at maximum brightness. They then compare these velocities to the light-curve shape parameter $\Delta m_{15}(B)$. Figure 2 presents the 44 SNe in the BSNIP data for which both v_0 and $\Delta m_{15}(B)$ are calculated. As above, the points are colour-coded by “Wang type” and shape-coded by Benetti type.

As in Figure 1, the FAINT objects are (by definition) found at the right-hand edge of Figure 2. Similarly, the HV objects are all in the upper half of the figure. All of the objects, except for a few of the highest velocity SNe and the object with the lowest velocity in the figure, are within $\sim 1500 \text{ km s}^{-1}$ of $11,000 \text{ km s}^{-1}$. This is remarkably similar to what was found by Hachinger et al. (2006), except the BSNIP data have a slightly larger scatter around the typical velocity of $\sim 11,000 \text{ km s}^{-1}$. Hachinger et al. (2006) also note that the majority of the scatter in velocity comes from the HVG objects, which is also true in Figure 2. However, there is a major difference between the two results. The BSNIP data in Figure 2 show that HVG SNe have a huge range of v_0 , spanning well above average to significantly below average values, whereas the data presented by Hachinger et al. (2006) exhibit evidence of the (oft-quoted) one-to-one relationship between HVG and HV SNe Ia. As mentioned in BSNIP II, while most HVG objects are found to have expansion velocities above the LVG objects, this is not an exclusive feature of HVG SNe Ia.

A relationship between the calculated intrinsic ‘‘pseudo-colour’’ $B_{\text{max}} - V_{\text{max}}$ (i.e., the B -band maximum minus the V -band maximum corrected for host-galaxy reddening) and v_0 has been seen previously (Foley et al. 2011). Figure 3 shows 39 BSNIP SNe for which we measure v_0 and the difference between observed B -band magnitude and observed V -band magnitude at the time of B -band maximum brightness (what we refer to as $(B - V)_{\text{max}}$ in this work). We opt to use (observed) $(B - V)_{\text{max}}$ since it is an actual, physical colour of the SN at a discrete period of time, though keep in mind that in this study we do not attempt to correct for host-galaxy reddening. Following Foley et al. (2011), we are only presenting SNe Ia with $(B - V)_{\text{max}} < 0.319 \text{ mag}$ in Figure 3.

The linear least-squares fit to all of the points is shown by the solid line. We see effectively no evidence for any overall correlation (Pearson correlation coefficient of 0.17^2), and the linear fit seems to be driven solely by the two outliers with $(B - V)_{\text{max}} > 0.25 \text{ mag}$. If those two objects are removed, the correlation coefficient drops to 0.05 (the best-fitting line to the remaining data is shown by the dotted line). Finally, the dashed line is the relationship between v_0 and $B_{\text{max}} - V_{\text{max}}$ from the model spectra of Kasen & Plewa (2007), as shown by Foley & Kasen (2011). When including all of the data in Figure 3, the correlation between v_0 and $(B - V)_{\text{max}}$ is weaker than what was seen by Foley et al. (2011), where they derive correlation coefficients of 0.28 and 0.39 for two different datasets.³ However, no correlation is present whatsoever if the two significant outliers are removed. The difference between the results shown here and those of Foley et al. (2011) is likely due to the fact that we do not correct the BSNIP colours for any possible host-galaxy reddening while Foley et al. (2011) attempt to convert the observed colours into intrinsic colours. We will

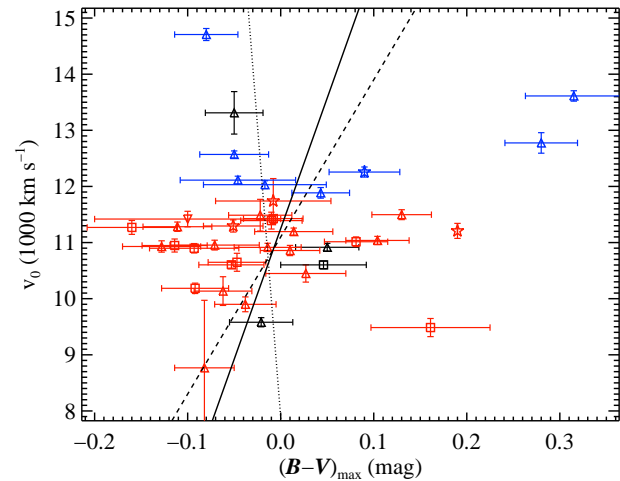


Figure 3. The velocity at maximum brightness of the Si II $\lambda 6355$ feature versus observed $(B - V)_{\text{max}}$ (i.e., the difference between observed B -band magnitude and observed V -band magnitude at the time of B -band maximum brightness) of 39 SNe. Colours and shapes of data points are the same as in Figure 1. The solid line is the fit to all of the data while the dotted line is the fit only to objects with $(B - V)_{\text{max}} < 0.25 \text{ mag}$. The dashed line is the relationship between v_0 and $B_{\text{max}} - V_{\text{max}}$ from the model spectra of Kasen & Plewa (2007), as shown by Foley & Kasen (2011).

delve deeper into this colour conversion in future BSNIP studies (Ganeshalingam et al., in preparation).

4.2.2 Velocities Near Maximum Brightness

If instead of v_0 we plot the actual measured velocity of the Si II $\lambda 6355$ feature for each object having a spectrum within 5 d of maximum brightness versus $\Delta m_{15}(B)$, the same basic trends are seen (but with nearly twice as many data points). A comparison of the velocity of the Si II $\lambda 5972$ feature (within 5 d of maximum brightness) with $\Delta m_{15}(B)$ yields nearly identical results. The biggest difference is that the velocities are clustered around $10,300 \text{ km s}^{-1}$, lower than that of the Si II $\lambda 6355$ feature. This difference between these features has been seen in previous studies as well (Hachinger et al. 2006). The same analysis using the velocity of the S II ‘‘W’’ once again shows the same behaviour, but with an even lower typical velocity ($\sim 9000 \text{ km s}^{-1}$). This has also been pointed out in earlier work (Hachinger et al. 2006). The velocity of the S II ‘‘W’’ feature is further discussed below.

Blondin et al. (2011) present a Hubble diagram that is corrected by SALT2 light-curve width parameter x_1 and colour parameter c in addition to the velocity of the Si II $\lambda 6355$ feature. This yielded approximately a 10 per cent decrease in the scatter of their Hubble diagram. It has also been shown that the Si II $\lambda 6355$ velocity is uncorrelated with both x_1 and c , and thus it gives information beyond light-curve width and colour. However, the anticorrelation of this velocity with Hubble residuals (corrected for light-curve width and colour) is relatively small (Blondin et al. 2011).

Plotted in Figure 4 are the 66 SNe Ia in the BSNIP sample which have SALT2 fits and measured Si II $\lambda 6355$

² The Pearson correlation coefficient is the correlation coefficient used throughout this work unless otherwise noted.

³ The first dataset, yielding a correlation coefficient of 0.28, comes from Wang et al. (2009) and includes some of the data used here. However, the two samples are distinct and the methods of velocity determination are significantly different.

velocities within 5 d of maximum brightness. The velocities are plotted against x_1 , c , and Hubble residuals corrected for light-curve width and colour (only for objects which are used to make the Hubble diagram). As above, the points are colour-coded by “Wang type.” In Figure 4 the data are shape-coded by what is referred to in BSNIP II as the “SNID type.” The SuperNova IDentification code (SNID; Blondin & Tonry 2007), as implemented in BSNIP I, was used to determine the spectroscopic subtype of each SN used in BSNIP II (as well as this study). SNID compares an input spectrum to a library of spectral templates in order to determine the most likely spectroscopic subtype. Spectroscopically normal objects are objects classified as “Ia-norm” by SNID.

The spectroscopically peculiar SNID subtypes used here include the often underluminous SN 1991bg-like objects (“Ia-91bg,” e.g., Filippenko et al. 1992b; Leibundgut et al. 1993), and the often overluminous SN 1991T-like objects (“Ia-91T,” e.g., Filippenko et al. 1992a; Phillips et al. 1992) and SN 1999aa-like objects (“Ia-99aa,” Li et al. 2001; Strolger et al. 2002; Garavini et al. 2004). See BSNIP I for more information regarding our implementation of SNID and the various spectroscopic subtype classifications. In Figure 4, Ia-norm objects are plotted as squares, Ia-91T objects are shown as upward-pointing triangles, Ia-99aa objects are displayed as downward-pointing triangles, and objects with no determined SNID subtype are circles.

The data in Figure 4 are extremely similar to those of Blondin et al. (2011) and show the same correlations (or lack thereof). The velocity of the Si II $\lambda 6355$ feature as measured from the BSNIP data is uncorrelated with x_1 (correlation coefficient -0.21). This velocity is also uncorrelated with c , as seen in Blondin et al. (2011). Removing SNe with $c > 0.5$ from the BSNIP data (which is done when Hubble diagrams are produced using this parameter) yields a correlation coefficient of 0.13 between Si II $\lambda 6355$ velocity and c .

The bottom panel of Figure 4 shows the velocity of the Si II $\lambda 6355$ feature versus the (x_1, c) -corrected Hubble residuals. If the correction term in a given model (here, the velocity of Si II $\lambda 6355$) is well correlated with the SALT2-corrected Hubble residuals, then the extra term is likely providing new information that is actually in the data. Thus, the model is improving the fit not by fitting to noise, but to physical information contained in the data. However, the correction term here is uncorrelated with the residuals (correlation coefficient 0.19).

No improvement is found (i.e., the WRMS increases) when adding the Si II $\lambda 6355$ velocity to the standard (x_1, c) model ($\Delta_{x_1, c} = 0.0083 \pm 0.0084$). Blondin et al. (2011) found that there was a $\lesssim 10$ per cent decrease in the WRMS when using the x_1 , c , and Si II $\lambda 6355$ velocity, but their $\Delta_{x_1, c}$ is consistent with 0 (as is ours). They also find only a “modest” correlation between Si II $\lambda 6355$ velocity and (x_1, c) -corrected residuals (correlation coefficient 0.4; Blondin et al. 2011). Therefore, it seems that adding the Si II $\lambda 6355$ velocity to the standard (x_1, c) model does *not* significantly improve the precision of SN Ia distance calculations.

In Figure 5 we plot all measured velocities of the Si II $\lambda 6355$ feature (within 5 d of maximum brightness) against $(B - V)_{\max}$. This differs from Figure 3 since the velocities in that plot were interpolated/extrapolated to $t = 0$ d (i.e., v_0) and this plot shows the actual velocities measured from the

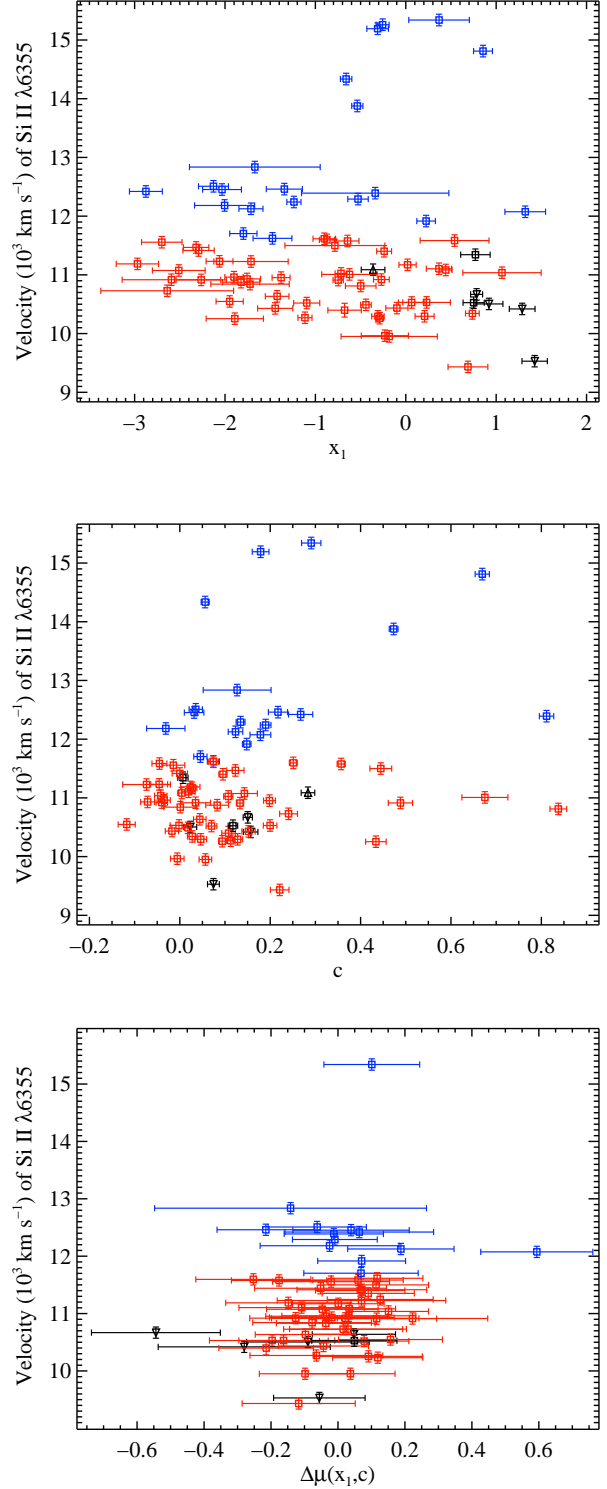


Figure 4. The velocity of the Si II $\lambda 6355$ feature versus SALT2 light-curve width parameter x_1 (top), SALT2 colour parameter c (middle), and Hubble residuals corrected for light-curve width and colour (bottom). Blue points are HV objects, red points are normal-velocity objects, and black points are objects for which we could not determine whether the SN was normal or high velocity. Squares are Ia-norm, upward-pointing triangles are Ia-91T, downward-pointing triangles are Ia-99aa, and circles are objects which do not have a SNID subtype (see BSNIP I for further details regarding how these subclasses are defined).

spectra. The top panel displays all 77 SNe from the BSNIP data for which both of these values have been measured and the bottom panel provides a close-up view of objects with $(B - V)_{\max} < 0.319$ mag (in order to match the sample fit by Foley et al. 2011).

The linear least-squares fit to all of the points is shown by the solid line and the fit to SNe with $(B - V)_{\max} < 0.319$ mag is shown by the dotted line; the correlation coefficients are 0.23 and 0.30, respectively, and slightly lower than the value found by Foley et al. (2011), 0.39 (though the linear fit shown here matches well to what was found in their study). As with Figure 3, there is only marginal evidence for a correlation and there is a large amount of scatter around the linear fit. Again, this is unsurprising since we are measuring *observed* $(B - V)_{\max}$ and Foley et al. (2011) are plotting pseudo-colours that have been corrected for host-galaxy reddening.

The typical $(B - V)_{\max}$ for HV objects is larger than for Ia-norm and Ia-91T/99aa, but smaller than that of Ia-91bg (which appear in the Figure as highly reddened, significant outliers). However, the range of $(B - V)_{\max}$ spanned by Ia-norm and HV objects is similar, with a significant amount of overlap. The scatter in $(B - V)_{\max}$ of the HV objects (0.098 mag) is effectively equal to that of the other objects in the bottom panel of Figure 5 (0.101 mag). While this matches the scatter in the HV objects found previously (0.095 mag; Foley et al. 2011), it differs from the SNe with velocities $< 11,800$ km s⁻¹, which they found to have a smaller intrinsic colour scatter (0.072 mag). The correction for host-galaxy reddening applied by Foley et al. (2011) is likely responsible for the decrease in colour scatter of the normal-velocity objects.

The dashed line in Figure 5 is the relationship between v_0 and $B_{\max} - V_{\max}$ from the model spectra of Kasen & Plewa (2007), as shown in Figure 8 of Foley & Kasen (2011). Interestingly, even though Foley et al. (2011) plot *intrinsic* colours and we plot *observed* colours, both studies match these predictions very well. One difference between Figure 5 and Figure 8 of Foley & Kasen (2011) is that the BSNIP data contain a handful of objects that are extremely reddened (i.e., they have relatively large values of $(B - V)_{\max}$). However, this can easily be explained. All of the Ia-norm and HV SNe in Figure 5 with $(B - V)_{\max} > 0.31$ mag have been observed to have significant reddening from their host galaxies (which is not taken into account in the models of Kasen & Plewa 2007). The other objects with $(B - V)_{\max} > 0.31$ mag are Ia-91bg, which were also not discussed in the models of Kasen & Plewa (2007).

Figure 8 of Foley & Kasen (2011) also presents the theoretical relationship between velocity of the Ca II H&K feature and intrinsic $(B - V)_{\max}$. A comparison of this velocity and observed $(B - V)_{\max}$ measured from the BSNIP data shows effectively no correlation with a correlation coefficient of only 0.14. Again, the scatter in $(B - V)_{\max}$ is similar for the HV and normal-velocity objects. However, this is unsurprising since, as pointed out in BSNIP II, the Ca II H&K velocities of HV and normal-velocity objects (determined using the Si II $\lambda 6355$ velocity) are highly overlapping.

A distance model involving x_1 , c , and the velocity of the Ca II H&K feature was calculated, and while the WRMS technically decreased with the addition of this velocity, it was not found to be significant ($\Delta_{x_1, c} = -0.0085 \pm 0.0141$).

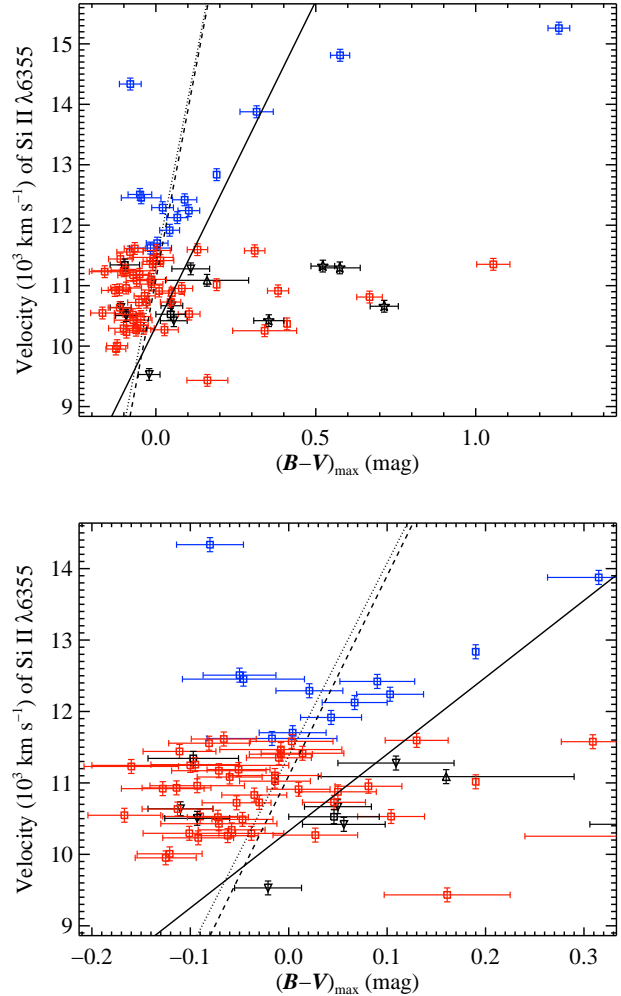


Figure 5. The velocity of the Si II $\lambda 6355$ feature versus observed $(B - V)_{\max}$ (top) and a close-up view of objects with $(B - V)_{\max} < 0.319$ mag (bottom). Blue points are HV objects, red points are normal-velocity objects, and black points are objects for which we could not determine whether the SN was normal or high velocity. Squares are Ia-norm, stars are Ia-91bg, upward-pointing triangles are Ia-91T, downward-pointing triangles are Ia-99aa, and circles are objects which do not have a SNID subtype (see BSNIP I for further details regarding how these subclasses are defined). The solid line is the fit to all of the data while the dotted line is the fit only to objects with $(B - V)_{\max} < 0.319$ mag. The dashed line is the relationship between v_0 and $B_{\max} - V_{\max}$ from the model spectra of Kasen & Plewa (2007), as shown by Foley & Kasen (2011).

Other models involving this velocity were all found to degrade the accuracy of distance measurements when compared to the standard (x_1, c) model.

Furthermore, we used Equations 4–7 along with velocities of all seven spectral features for which velocities were measured and compared the results to the (x_1, c) model. The vast majority of these models predicted a larger scatter than the standard model corrected for light-curve width and colour. However, both the O I $\lambda 7773$ triplet and the Ca II near-IR triplet, when combined with x_1 and c , were

found to perform equally as well as when using just x_1 and c . Thus, adding either of these velocities did not degrade the distances calculated, but they did not significantly improve them either.

On the other hand, the velocity of the S II ‘‘W,’’ when used in conjunction with x_1 and c , decreased the WRMS by ~ 3 per cent and the σ_{pred} by ~ 14 per cent, at the 1.8σ level ($\Delta_{x_1,c} = -0.0119 \pm 0.0066$). Figure 6 shows the 64 SNe Ia in the BSNIP sample which have SALT2 fits and measured S II ‘‘W’’ velocities within 5 d of maximum brightness. The velocities are again plotted against x_1 , c , and Hubble residuals corrected for light-curve width and colour (only for SNe that are part of the Hubble diagram).

Neither x_1 nor c show any correlation with the velocity of the S II ‘‘W’’ (correlation coefficients of 0.13 and 0.17, respectively). Even when removing SNe with $c > 0.5$ from the BSNIP data (as done for the Hubble diagrams), the correlation coefficient becomes only -0.15 . The bottom panel of Figure 6 shows the velocity of the S II ‘‘W’’ versus the (x_1, c) -corrected Hubble residuals. The correction term is uncorrelated with the residuals (correlation coefficient 0.003). Figure 7 shows the actual Hubble diagram residuals for this model (top panel) as well as the standard (x_1, c) model (using the same set of objects; bottom panel) versus redshift. Also shown, as the grey band, is the WRMS for both models.

While the relative depth of this feature has been seen to improve Hubble diagrams (Blondin et al. 2011, and Section 4.3 of this work), the velocity of this feature has not previously been shown to do this. When adding the velocity of the S II ‘‘W’’ feature to the standard (x_1, c) model, the overall decrease in WRMS is relatively small, but the effect appears to be fairly significant. This distance model should be explored further using future, larger datasets.

4.3 Relative Depths

The depth of the *bluer absorption* of the S II ‘‘W’’ feature relative to the pseudo-continuum has been shown to decrease the scatter of Hubble residuals by about 10 per cent (Blondin et al. 2011). The relative depth (a) of this feature was found to be uncorrelated with both x_1 and c by Blondin et al. (2011), and its correlation with Hubble residuals (corrected for light-curve width and colour) is relatively small. Figure 8 presents the 64 BSNIP SNe Ia which have SALT2 fits and measured relative depths of the *redder absorption* of the S II ‘‘W’’ feature within 5 d of maximum brightness. The depths are plotted against x_1 , c , and Hubble residuals corrected for light-curve width and colour (for objects that are in the Hubble diagram). It should be noted that whereas Blondin et al. (2011) measure the bluer absorption of this feature ($\lambda 5454$), we measure only the redder absorption ($\lambda 5624$) in BSNIP II. While these absorptions are separated by $< 200 \text{ \AA}$, there may be differences between the relative depths of the two. Nevertheless, we will compare the results presented here to those of Blondin et al. (2011), with the caveat that this may be analogous to comparing ‘‘Red Delicious apples’’ to ‘‘Granny Smith apples.’’

The BSNIP data show a fairly significant correlation between the relative depth of S II ‘‘W’’ and x_1 (a correlation

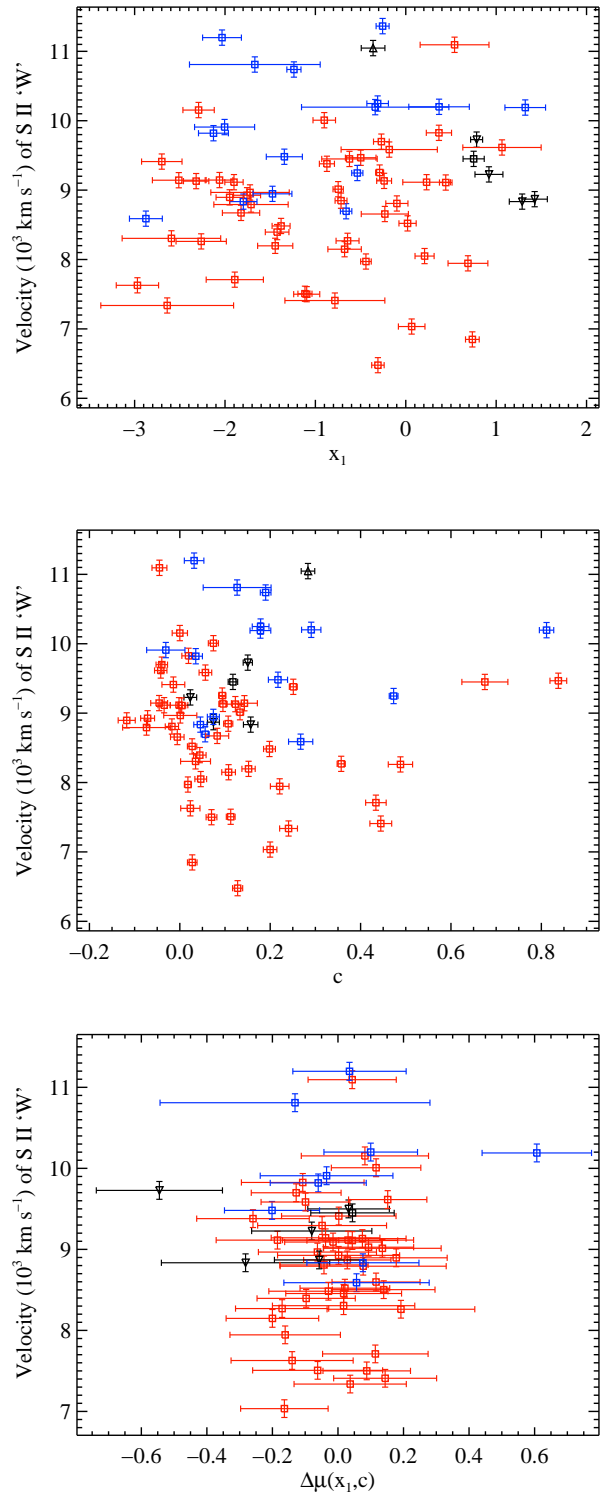


Figure 6. The velocity of the S II ‘‘W’’ feature versus SALT2 light-curve width parameter x_1 , SALT2 colour parameter c , and Hubble residuals corrected for light-curve width and colour. Colours and shapes of data points are the same as in Figure 5.

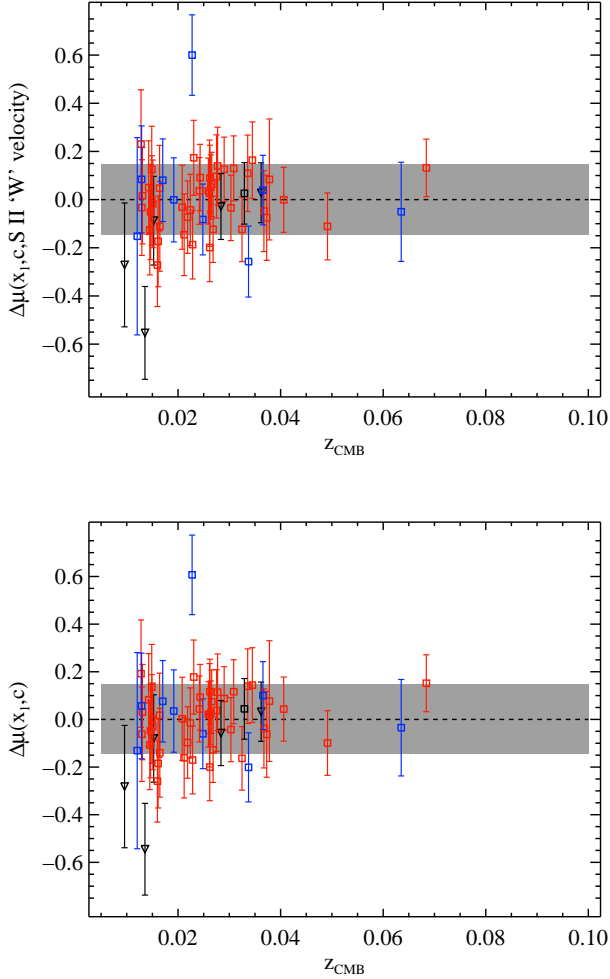


Figure 7. Hubble diagram residuals versus z_{CMB} for the $(x_1, c, \text{S II 'W' velocity})$ model (*top*) and the standard (x_1, c) model (Equation 8, *bottom*). The grey band is the WRMS for each model. Colours and shapes of data points are the same as in Figure 5.

coefficient of -0.47 , which is significant at the $> 3\sigma$ level⁴). This is in stark contrast to Blondin et al. (2011), who found no evidence of such a correlation (correlation coefficient -0.04). As opposed to x_1 , both studies agree that c is uncorrelated with the relative depth a of the S II “W” feature (the BSNIP data having a correlation coefficient of 0.09). The Hubble residuals corrected for x_1 and c show weak evidence of a correlation with the relative depth of the S II “W” (correlation coefficient 0.29). Blondin et al. (2011) found that a model which includes x_1 , c , and a of the S II “W” will decrease the WRMS by $\lesssim 10$ per cent, while we find the

⁴ This significance comes from using the Pearson correlation coefficient for each correlation tested in this study to calculate a p -value. This value tests the null hypothesis that there is no correlation versus the alternative that a correlation exists. Then, based on the p -values of all of the tested correlations, we calculate the 3σ cutoff by employing the False-Discovery Rate Method (Miller et al. 2001).

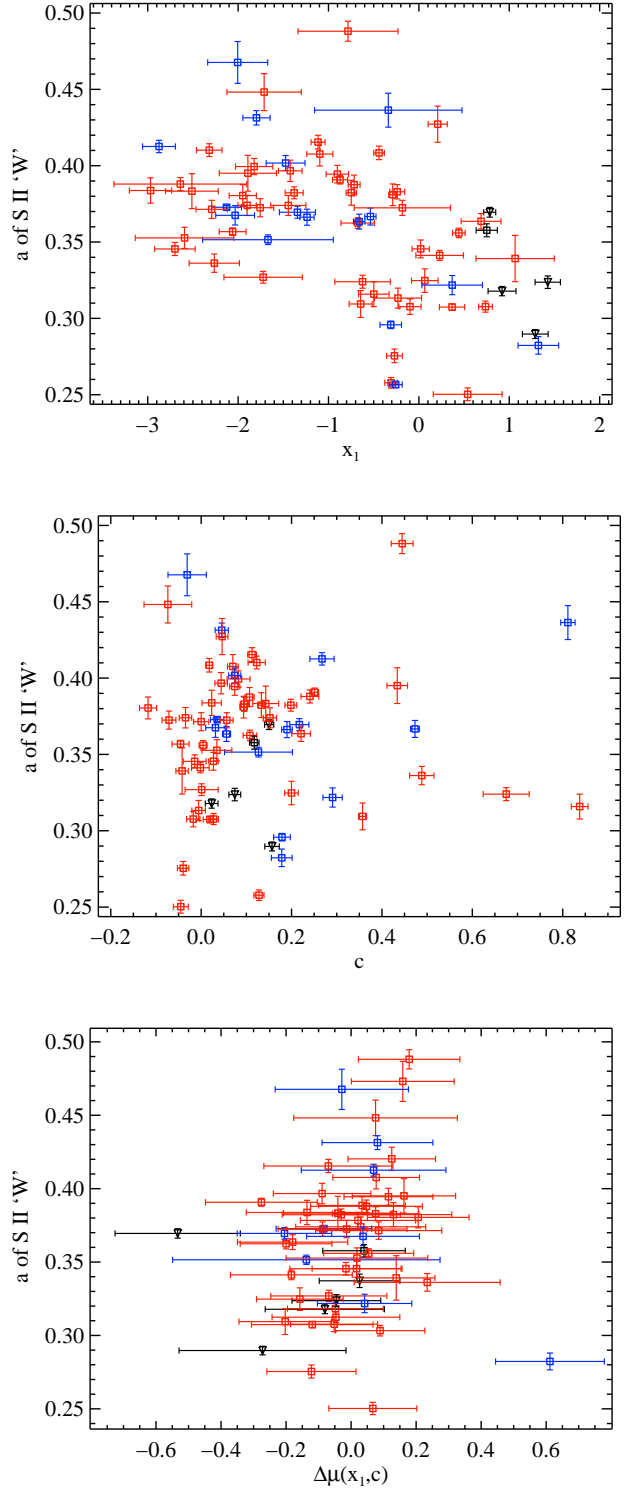


Figure 8. The relative depth of the S II “W” feature versus SALT2 light-curve width parameter x_1 (*top*), SALT2 colour parameter c (*middle*), and Hubble residuals corrected for light-curve width and colour (*bottom*). Colours and shapes of data points are the same as in Figure 5.

WRMS to be effectively unchanged whether or not one adds in the relative depth of Si II “W” ($\Delta_{x_1,c} = 0.0012 \pm 0.0047$).

All other spectral features’ relative depths were used, along with Equations 4–7, to create Hubble diagrams. No model significantly decreased the residuals over the standard (x_1, c) model. Models involving the relative depth of Ca II H&K, Si II $\lambda 6355$, and the O I triplet, each in combination with x_1 and c , were found to be as accurate as the (x_1, c) model.

4.4 Pseudo-Equivalent Widths

Nordin et al. (2011b) fit the temporal evolution of their pEW measurements to attempt to “remove” the age dependence of the pEW values. To do this, an epoch-independent quantity called the “pEW difference” (ΔpEW) was defined; it is simply the measured pEW minus the expected pEW at the same epoch using the linear or quadratic fit. In BSNIP II we calculated ΔpEW for the BSNIP sample. However, the relationships seen in BSNIP II involving ΔpEW values were also seen when simply using the pEW values (within 5 d of maximum brightness). This is due to the fact that pEWs do not evolve much within a few days of maximum. Furthermore, the ΔpEW values rely on defining a fit to the measurements which adds another assumption to the analysis. Thus, the current study will focus solely on pEW values within 5 d of maximum brightness and will not further investigate ΔpEW values. Note that comparisons to Nordin et al. (2011b) will be made, despite the fact that their study uses ΔpEW values almost exclusively.

4.4.1 Si II $\lambda 4000$

The pEW of the Si II $\lambda 4000$ feature has recently been found to be an indicator of light-curve width due its relatively tight anticorrelation with the SALT2 x_1 parameter (Arsenijevic et al. 2008; Walker et al. 2011; Blondin et al. 2011; Nordin et al. 2011b; Chotard et al. 2011). Curiously, in BSNIP II, only a weak correlation was found between this pEW and another often-used SN Ia luminosity indicator, the so-called “Si II ratio”, $\mathcal{R}(\text{Si II})$ (originally defined by Nugent et al. 1995; see also BSNIP II and Section 4.5 for more information on this spectral parameter). Here the pEW of Si II $\lambda 4000$ is compared directly to photometric parameters.

In Figure 9 we present the 57 BSNIP SNe which have SALT2 fits and measured pEW values for the Si II $\lambda 4000$ feature within 5 d of maximum brightness. The pEWs are plotted against x_1 , c , and Hubble residuals corrected only for colour (for SNe Ia that are used when constructing the Hubble diagram).

The pEW of Si II $\lambda 4000$ is highly correlated with x_1 (Figure 9, top plot) with a correlation coefficient of -0.86 (which is significant at $> 3\sigma$). This is in agreement with many previous studies and is actually a stronger correlation than has been seen before (e.g., Arsenijevic et al. 2008; Walker et al. 2011; Blondin et al. 2011; Nordin et al. 2011b; Chotard et al. 2011). The least-squares linear fit to the data is shown as the solid line in the top plot of Figure 9 (the dashed lines are the standard error of the fit). Note that the Ia-99aa objects in the figure also lie along the relationship.

Arsenijevic et al. (2008) plotted x_1 versus the pEW of

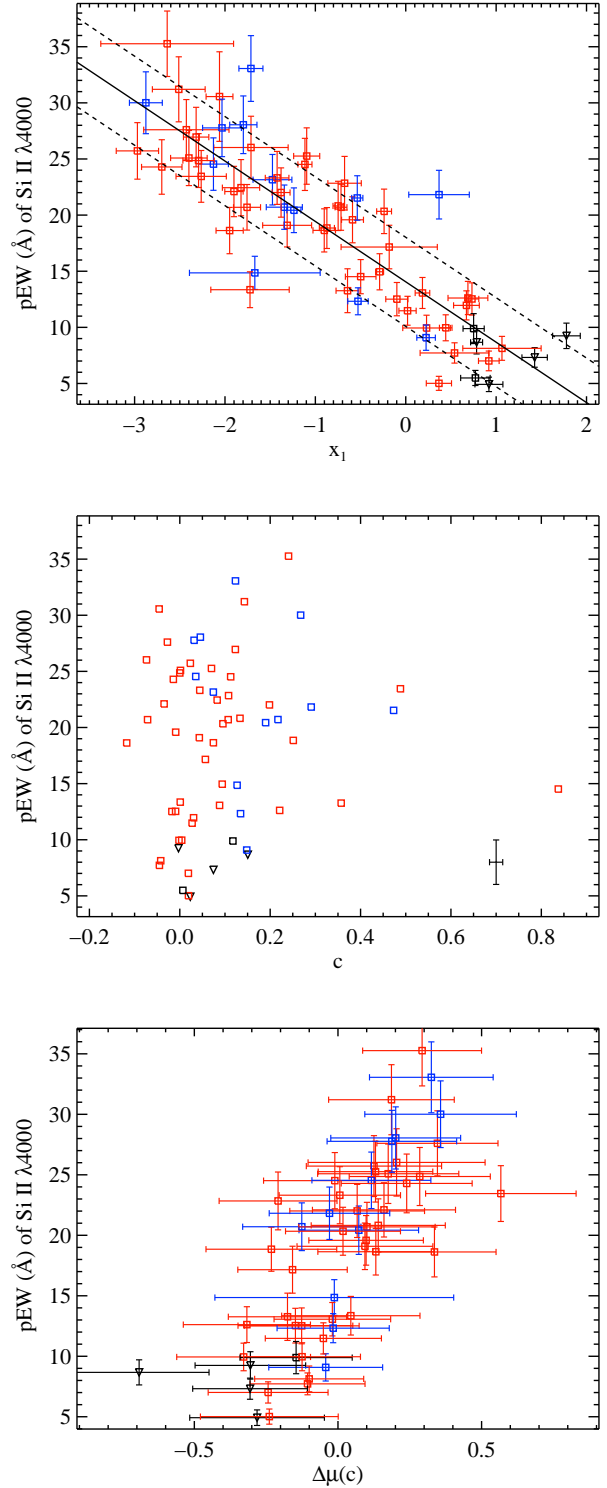


Figure 9. The pEW of the Si II $\lambda 4000$ feature versus SALT2 light-curve width parameter x_1 (*top*), SALT2 colour parameter c (*middle*), and Hubble residuals corrected for colour only (*bottom*). Colours and shapes of data points are the same as in Figure 5. In the top plot, the solid line is the linear least-squares fit and the dashed lines are the standard error of the fit. In the middle plot, the median uncertainty in both directions is shown in the lower-right corner.

Si II $\lambda 4000$ and coded each low-redshift point based on its Benetti type; they found that the FAINT objects fell below the linear relationship (i.e., they had smaller than expected pEW values). In BSNIP II it was shown that FAINT (and similarly, Ia-91bg) objects have, if anything, *larger* than average pEW values (especially for the Si II $\lambda 4000$ feature). Figure 9 shows no Ia-91bg objects since SALT/2 is unable to fit that spectral subtype. However, when the BSNIP values of x_1 are plotted against the pEW of Si II $\lambda 4000$ and coded by Benetti type, the two FAINT objects fall at the upper-left end of the linear correlation. The cause of this discrepancy between the two studies is unclear.

The middle plot of Figure 9 shows no real evidence that the pEW of the Si II $\lambda 4000$ feature is correlated with c . The correlation coefficient we find for all of the objects is 0.095, and when removing objects with $c > 0.5$, the coefficient only increases to 0.20. This is slightly smaller than what was found by Blondin et al. (2011), and significantly smaller than what was found by Nordin et al. (2011a). While the former claim no observed correlation, the latter do claim that the pEW of Si II $\lambda 4000$ is correlated with c .

The bottom panel of Figure 9 shows the Hubble residuals when corrected only for SALT2 colour versus the pEW of Si II $\lambda 4000$. Blondin et al. (2011) saw a relatively weak correlation between these parameters and found that a distance model involving c and the pEW of the Si II $\lambda 4000$ feature led to a “marginal improvement” over the standard (x_1, c) model. We find a strong correlation (coefficient of 0.81, significant at $> 3\sigma$), and the $(c, \text{Si II } \lambda 4000 \text{ pEW})$ model performs nearly as well as the (x_1, c) model ($\Delta_{x_1, c} = 0.012 \pm 0.036$). Thus, the BSNIP data are in agreement with the finding of Blondin et al. (2011) that the pEW of the Si II $\lambda 4000$ feature is essentially a replacement for the x_1 parameter and is an accurate measurement of light-curve width. Figure 10 shows the Hubble diagram residuals for the $(c, \text{Si II } \lambda 4000 \text{ pEW})$ model and the colour-corrected-only model versus redshift, with the WRMS for each model as the grey band.

Interestingly, we found that a model involving c , x_1 , and the pEW of the Si II $\lambda 4000$ feature actually leads to a ~ 10 per cent decrease in WRMS and a ~ 28 per cent decrease in σ_{pred} . For this model, $\Delta_{x_1, c} = -0.026 \pm 0.15$, which implies that the improvement has a significance of about 1.8σ . The correlation between pEW of Si II $\lambda 4000$ and Hubble residuals corrected for colour and light-curve width is only 0.20, and thus perhaps the combination of c , x_1 , and pEW of the Si II $\lambda 4000$ feature is not actually adding much new information. However, the utility of a model including all three of these parameters should be investigated with other SN samples. Figure 11 contains Hubble residuals for the $(x_1, c, \text{Si II } \lambda 4000 \text{ pEW})$ model as well as the standard (x_1, c) model (using the same set of objects) versus redshift. Also shown, as the grey band, is the WRMS for each model.

While the above investigation focused on the SALT2 light-curve fitter, we can investigate correlations between the pEW of the Si II $\lambda 4000$ feature and photometric parameters from MLCS2k2. Figure 12 shows the 63 BSNIP SNe which have MLCS2k2 fits and measured pEW values for the Si II $\lambda 4000$ feature within 5 d of maximum brightness. The pEWs are plotted against Δ and A_V .

The correlation coefficient between pEW of Si II $\lambda 4000$ and Δ is 0.74, which is larger than previously observed

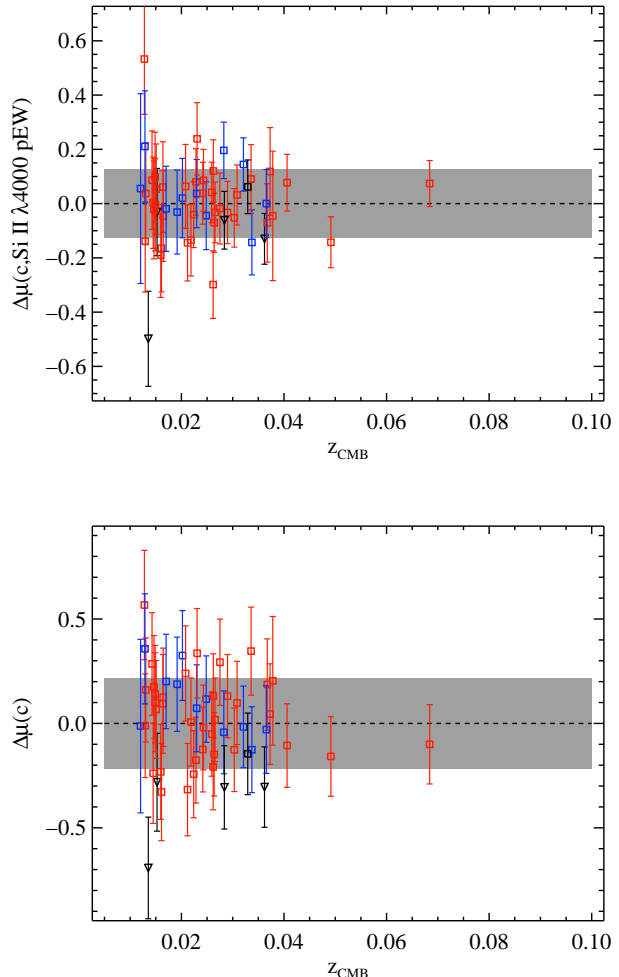


Figure 10. Hubble diagram residuals versus z_{CMB} for the $(c, \text{Si II } \lambda 4000 \text{ pEW})$ model (*top*) and the colour-corrected-only model (*bottom*). The grey band is the WRMS for each model. Colours and shapes of data points are the same as in Figure 5.

(Nordin et al. 2011b) and implies that these parameters are highly correlated (at a significance $> 3\sigma$). This is expected based on the high degree of correlation between the pEW of Si II $\lambda 4000$ and x_1 since both Δ and x_1 are measurements of the width of SN Ia light curves. In Figures 12 and 9 the Ia-99aa objects lie at the extreme low-pEW end of the relationship, though perhaps they are slightly systematically below the trend in the top panel of Figure 12. On the other hand, the Ia-91bg objects in the top panel of Figure 12 fall significantly below the linear trend.

As in Nordin et al. (2011b), there is no significant correlation between the pEW of Si II $\lambda 4000$ and A_V , even when objects with $A_V > 0.5$ mag are removed (correlation coefficients of < 0.13 in both cases using the BSNIP data). In all of the plots presented in this section, HV and Ia-norm objects overlap significantly. This is expected since in BSNIP II it was shown that the pEW of the Si II $\lambda 4000$ feature is extremely similar for these two subclasses. We also note that the plot of $\Delta m_{15}(B)$ versus the pEW of Si II $\lambda 4000$ looks

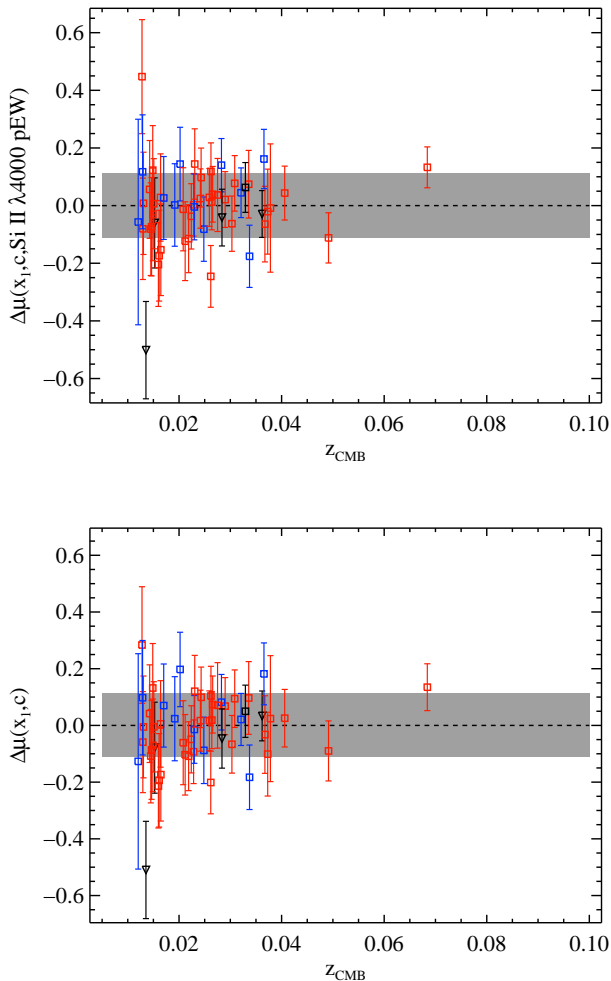


Figure 11. Hubble diagram residuals versus z_{CMB} for the $(x_1, c, \text{Si II } \lambda 4000 \text{ pEW})$ model (*top*) and the standard (x_1, c) model (*bottom*). The grey band is the WRMS for each model. Colours and shapes of data points are the same as in Figure 5.

nearly identical to the top panel of Figure 12 and has a larger correlation coefficient of 0.85 (again, significant at $> 3\sigma$).

4.4.2 Fe II and Mg II

Nordin et al. (2011b) found that the ΔpEW of Fe II within 3 d of maximum brightness is well correlated with SALT colour. In Figure 13 we present the 63 SNe in the BSNIP sample which have SALT2 fits and a measurement of the pEW of the Fe II complex within 5 d of maximum brightness. The two observables plotted have a correlation coefficient of 0.49 (with significance $> 3\sigma$), increasing slightly for objects with $c < 0.5$. If, however, only spectra within 3 d of maximum brightness are used, the correlation increases slightly but the sample size decreases by nearly one-quarter. The strength of this correlation is slightly higher than that found by Nordin et al. (2011b), though we point out that they used SALT colour while we use SALT2 colour, and they used ΔpEW (i.e., the difference between the measured pEW and the average pEW evolution) while we use the ac-

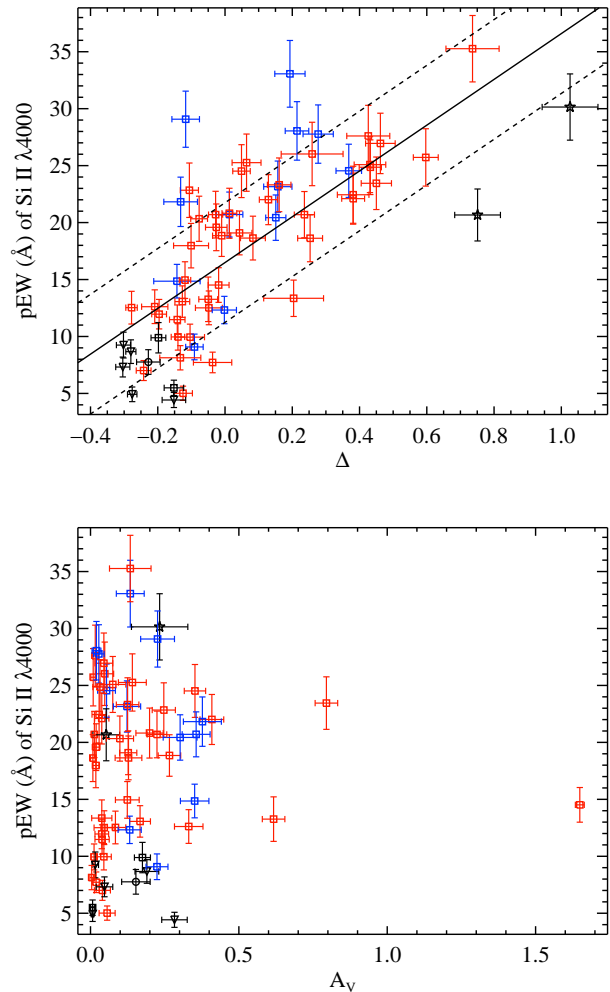


Figure 12. The pEW of the Si II $\lambda 4000$ feature versus MLCS2k2 light-curve width parameter Δ (*top*) and MLCS2k2 reddening parameter A_V (*bottom*). Colours and shapes of data points are the same as in Figure 5. In the top plot, the solid line is the linear least-squares fit and the dashed lines are the standard error of the fit.

tual measured pEW. Ia-99aa objects appear to have typical values of both the pEW of Fe II and c , though there are a very small number of objects of this spectral subtype. On the other hand, HV SNe seem to be both redder and have larger pEWs, but as before, there is significant overlap with Ia-norm objects as well.

The pEW of the Mg II complex is also correlated with c , as seen in Figure 14. In that figure, 64 SNe within 5 d of maximum brightness are plotted, and they have a correlation coefficient of 0.44 (for objects with $c < 0.5$) with the significance of the correlation $\sim 3\sigma$. Once again, when using only spectra within 3 d of maximum brightness the correlation becomes slightly stronger at the expense of significant decrease in the sample size. This correlation has been observed previously, though at slightly lower significance and with about one-third the number of low- z SNe (Walker et al. 2011). The data presented in Figure 14 match well with what was shown by Walker et al. (2011) for low- z objects, but their high- z sample spans a much larger range

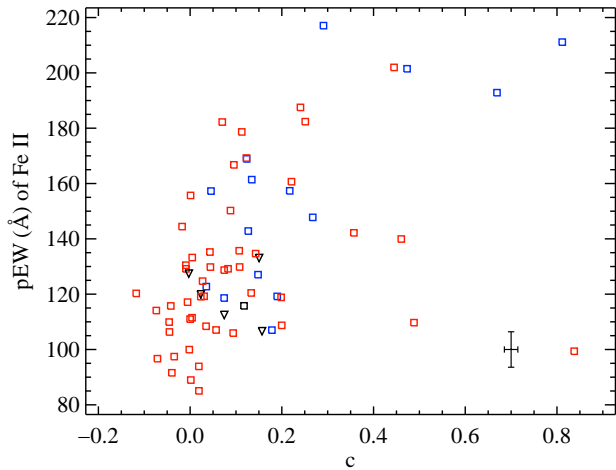


Figure 13. The pEW of the Fe II complex versus the SALT2 colour parameter c . Colours and shapes of data points are the same as in Figure 5. The median uncertainty in both directions is shown in the lower-right corner.

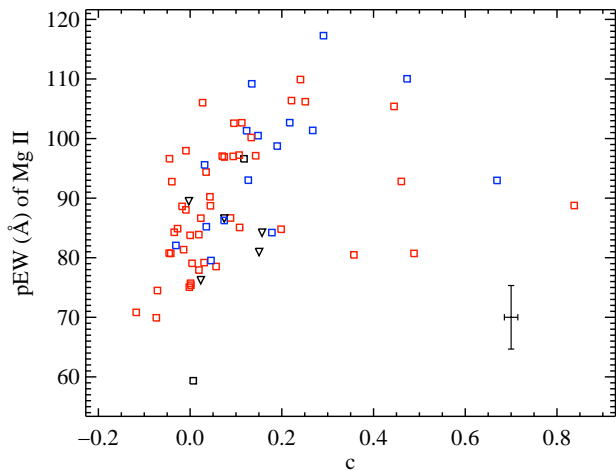


Figure 14. The pEW of the Mg II complex versus the SALT2 colour parameter c . Colours and shapes of data points are the same as in Figure 5. The median uncertainty in both directions is shown in the lower-right corner.

of Mg II pEW values and shows nearly no correlation with c . There seems to be effectively no difference between the various spectroscopic subtypes in this parameter space.

The significant correlations between c and both the pEWs of Mg II and Fe II are promising. Measuring a pEW of a broad feature in a single spectrum near maximum brightness is much simpler than obtaining photometric data for a full light curve that needs to then be modeled by a light-curve fitter (such as SALT2). Furthermore, since interstellar reddening cannot affect pEWs significantly, it seems that the *intrinsic* colour of the SN is correlated with both the pEWs of Mg II and Fe II.

As with all other spectral measurements discussed in this work, we constructed Hubble diagrams using the pEW of Mg II and Fe II and models of the form shown in Equa-

tions 4–7. All but one of these models performed worse than the standard (x_1, c) model. The model including x_1 , c , and the pEW of Mg II was only as accurate as the standard model ($\Delta_{x_1, c} = -0.004 \pm 0.004$). However, using the pEW of Mg II or Fe II as a replacement for c or in addition to c (along with x_1) is a tantalising possibility that should be explored using future datasets.

Furthermore, we attempt two Hubble diagrams using no light-curve information whatsoever. One uses only the pEWs of the Si II $\lambda 4000$ feature and the Mg II complex, and the other uses only the pEWs of the Si II $\lambda 4000$ feature and the Fe II complex. The idea is that the pEW of Si II $\lambda 4000$ is a good proxy for x_1 , and the pEWs of the Mg II and Fe II features are reasonably good proxies for c . These Hubble diagrams included only a subset of the data used in the flux-ratio study (see Section 4.10) since they needed to have well-measured pEWs. While both the Mg II and Fe II models had quite low WMRS values (0.274 and 0.297, respectively), they were not as low as the WRMS values using the standard (x_1, c) model (0.118 and 0.121, respectively).

4.4.3 S II “W”

As discussed in Section 4.3, the depth of the *bluer absorption* of the S II “W” feature relative to the pseudo-continuum was shown by Blondin et al. (2011) to decrease the scatter of Hubble residuals by about 10 per cent. In that section we showed that the relative depths of the *redder absorption* of the S II “W” in the BSNIP data were marginally correlated with x_1 , opposite to what was seen by Blondin et al. (2011). However, both studies agree that c and the colour- and width-corrected Hubble residual are uncorrelated with the relative depth of the S II “W.”

As discussed in BSNIP II, the relative depth of a spectral feature relies on a spline fit to the spectra and can fairly easily be contaminated by local noise. The pEW, however, is less prone to this type of contamination, relies only on the definition of the pseudo-continuum (and not any additional fit to the data), and often contains the same information as the relative depth. For these reasons the pEW values were used in favor of the a values in the analysis performed in BSNIP II. Furthermore, both Blondin et al. (2011) and BSNIP II measure the pEW of the *entire* S II “W” feature, and thus pEW values are a more fair comparison between the two studies than are the a values.

We find that c is uncorrelated with the pEW of the S II “W” (correlation coefficient of 0.15 for objects with $c < 0.5$). In contrast with the relative depth of the S II “W,” however, x_1 is *also* uncorrelated with the pEW of the S II “W” (correlation coefficient -0.16). This is significantly weaker than the correlation between x_1 and the relative depth of this feature found in Section 4.3. Equations 4–7 were used to create Hubble diagrams involving the pEW of the S II “W,” but none of these models led to an improvement in the WRMS.

4.4.4 Si II $\lambda 5972$

In BSNIP II it was shown that the pEW of the Si II $\lambda 5972$ feature correlated well with the spectral luminosity indicator $\Re(\text{Si II})$ (see Section 4.5 for more information on this parameter). Thus, one might expect this pEW to be an accurate luminosity indicator as well, and in fact evidence for

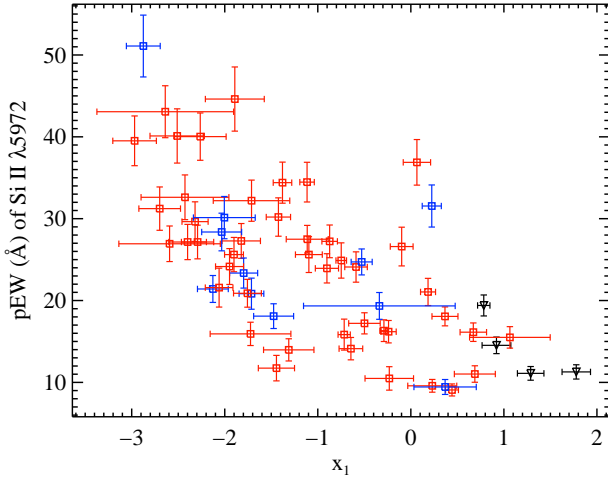


Figure 15. The pEW of Si II $\lambda 5972$ versus the SALT2 light-curve width parameter x_1 . Colours and shapes of data points are the same as in Figure 5.

a correlation between the pEW of Si II $\lambda 5972$ and both x_1 and $\Delta m_{15}(B)$ has been seen in previous work (Nordin et al. 2011b; Hachinger et al. 2006).

Figure 15 shows the 55 SNe which have a SALT2 fit as well as a measured pEW for the Si II $\lambda 5972$ feature. We find a correlation coefficient of -0.66 with a significance of $> 3\sigma$, which is stronger than what was found by Nordin et al. (2011b). As in the relationship between x_1 and the pEW of Si II $\lambda 4000$, the Ia-99aa objects appear to follow the relation.

Similarly, a strong linear correlation has been observed between the pEW of Si II $\lambda 5972$ and $\Delta m_{15}(B)$ (Hachinger et al. 2006). This relationship is also found in the BSNIP data, as shown in Figure 16: there are 62 SNe, the parameters have a correlation coefficient of 0.76 (significant at $> 3\sigma$), and as with the relationship with x_1 , Ia-99aa objects occupy the bottom of the correlation while the Ia-norm and HV objects are highly overlapping.

Hachinger et al. (2006) denote the Benetti type of each object on their plot of the pEW of Si II $\lambda 5972$ versus $\Delta m_{15}(B)$ and note that FAINT objects are found at the top of the correlation while LVG SNe are found at the bottom (with most HVG objects occupying the middle of the trend). The BSNIP data show a similar behaviour for the FAINT objects (again, much like the Ia-91bg objects in Figure 16); however, our data show no differentiation between the LVG and HVG objects in this parameter space.

Finally, we note that when plotting the pEW of the Si II $\lambda 5972$ feature against the MLCS2k2 Δ parameter, nearly the exact same results are seen as those in Figure 16. As with the S II “W,” no distance model utilising the pEW of Si II $\lambda 5972$ led to an improvement in the Hubble residuals.

4.4.5 Si II $\lambda 6355$

Much like the pEW of Si II $\lambda 5972$, the pEW of Si II $\lambda 6355$ has been seen to correlate marginally well with x_1 and to separate various spectral subtypes when compared to

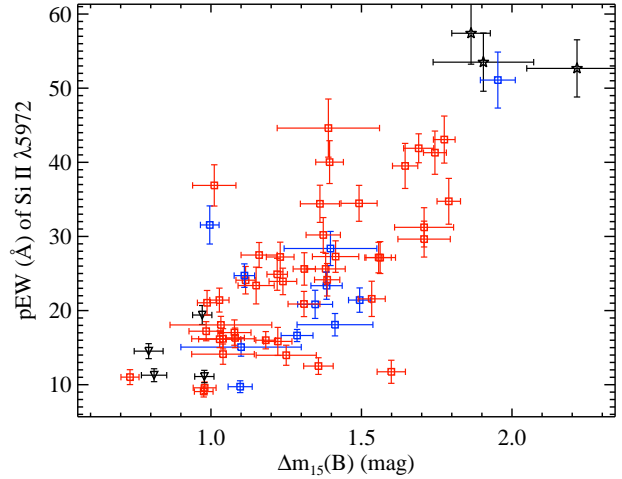


Figure 16. The pEW of the Si II $\lambda 5972$ feature versus $\Delta m_{15}(B)$. Colours and shapes of data points are the same as in Figure 5.

$\Delta m_{15}(B)$ (Nordin et al. 2011b; Hachinger et al. 2006, respectively).

In Figure 17 the 66 SNe with SALT2 fits and pEW values for the Si II $\lambda 6355$ feature are shown. The pEW values are plotted against x_1 , c , and Hubble residuals corrected for light-curve width and colour (for objects that are part of the Hubble diagram). A correlation coefficient of -0.58 is calculated for the top panel, which is significant at $> 3\sigma$. This is consistent with what was observed in the data studied by Nordin et al. (2011b). As in the previous two relationships between x_1 and the pEW of Si II features, the Ia-99aa objects follow the linear relation.

We find that c is somewhat correlated with the pEW of Si II $\lambda 6355$ (correlation coefficient of 0.43 and significance of $\sim 3\sigma$) for objects with $c < 0.5$. This pEW is even less correlated with Hubble residuals corrected for x_1 and c (correlation coefficient 0.23). A distance model which includes x_1 , c , and the pEW of the Si II $\lambda 6355$ feature leads to a 4 per cent decrease in WRMS, a 6 per cent decrease in σ_{pred} , and is significant at the 1.2σ level. So while this is technically an improvement over the standard (x_1, c) model, it may not actually be very helpful.

Plotting the pEW of Si II $\lambda 6355$ versus $\Delta m_{15}(B)$, Hachinger et al. (2006) are able to separate FAINT, LVG, and HVG objects relatively accurately. This is also seen, though at a lower significance, in the BSNIP data. In Figure 18 we plot 80 SNe; the parameters have a correlation coefficient of 0.45 (again with a significance of $\sim 3\sigma$), but the Ia-91bg, Ia-99aa, and the lone Ia-91T objects are all reasonably well separated from the bulk of the SNe. There is even some evidence for a difference between HV and Ia-norm objects in this parameter space. As mentioned above, Hachinger et al. (2006) denote the Benetti type of each object on their plot of the pEW of Si II $\lambda 6355$ versus $\Delta m_{15}(B)$ and state that the three subtypes are well separated. Again the BSNIP data support this conclusion, but at a weaker significance. FAINT objects are found in the same part of parameter space as the Ia-91bg objects, while HVG and HV SNe tend to occupy a different part of parameter space compared with the LVG and Ia-norm/91T/99aa objects. How-

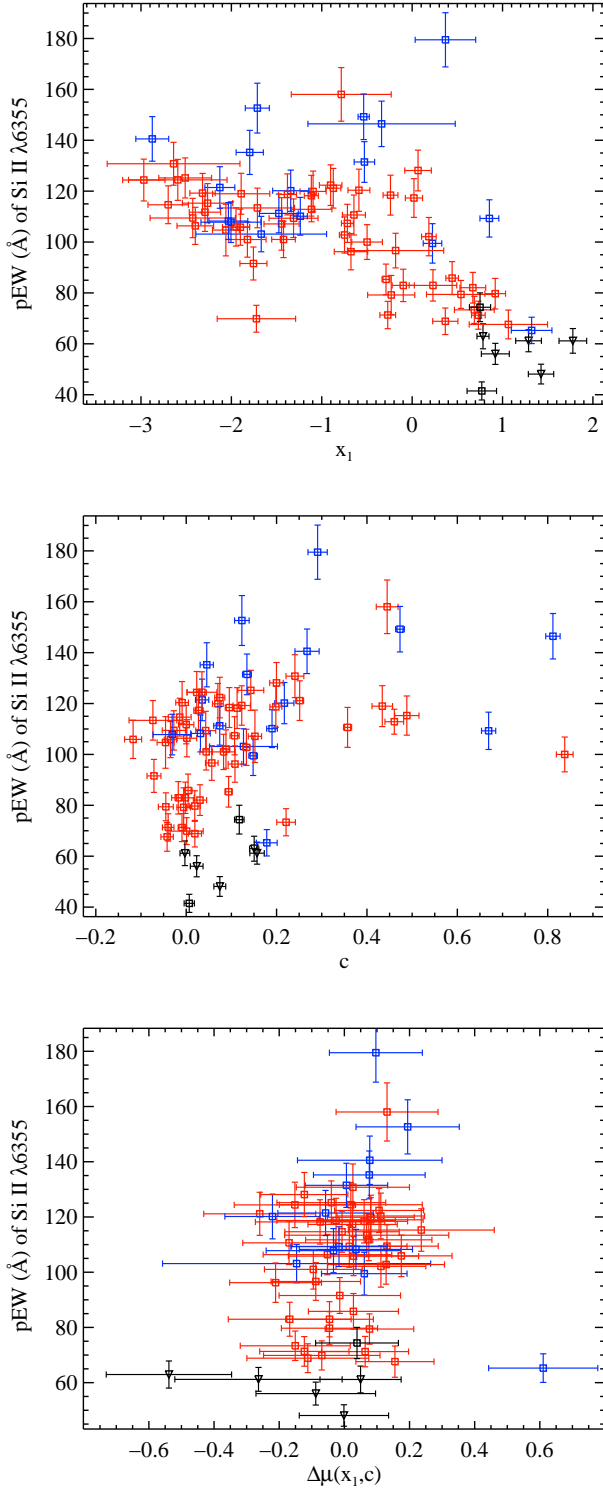


Figure 17. The pEW of the Si II $\lambda 6355$ feature versus SALT2 light-curve width parameter x_1 (*top*), SALT2 colour parameter c (*middle*), and Hubble residuals corrected for light-curve width and colour (*bottom*). Colours and shapes of data points are the same as in Figure 5.

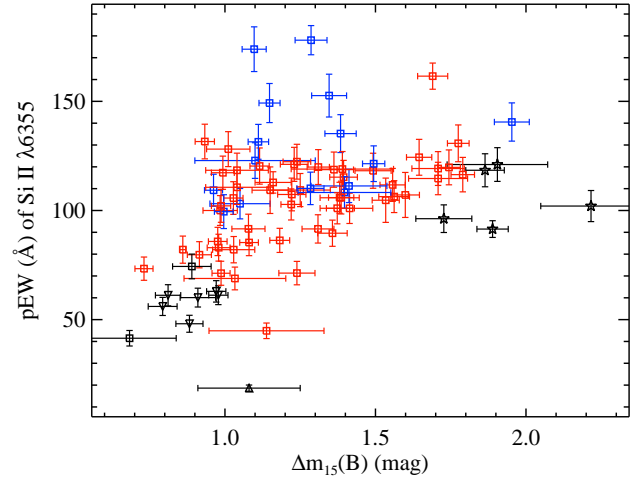


Figure 18. The pEW of Si II $\lambda 6355$ versus $\Delta m_{15}(B)$. Colours and shapes of data points are the same as in Figure 5.

ever, there is quite a lot of overlap among all of the non-FAINT (and non-Ia-91bg) SNe.

Figure 19 presents the pEW of the Si II $\lambda 6355$ feature plotted against $(B - V)_{\max}$. The top panel shows all 78 SNe from the BSNIP dataset for which both of these values have been measured and the bottom panel displays a close-up view of objects with $(B - V)_{\max} < 0.319$ mag. The linear least-squares fit to all of the points is represented by the solid line, and the fit to SNe with $(B - V)_{\max} < 0.319$ mag is shown by the dotted line.

The correlations for the full sample and the less reddened sample are weak (coefficients 0.12 and 0.16, respectively). Qualitatively, this matches the work of Foley et al. (2011), even though they plot *intrinsic* colours and we plot *observed* colours. The pEW of the Si II $\lambda 6355$ feature is less correlated with observed $(B - V)_{\max}$ than the velocity near maximum brightness of that same spectral feature.

4.4.6 Ca II and O I

Much like Hachinger et al. (2006), we searched for possible correlations between the pEW of each spectral feature investigated and various photometric parameters. Many of the strongest and most interesting of these possible correlations have been discussed in the preceding sections. For Ca II H&K as well as the O I triplet, no pairs of pEWs and photometric parameters were found to have correlation coefficients > 0.4 .

However, the pEW of the Ca II near-IR triplet is found to correlate with Δ (with a correlation coefficient of 0.66 and significance of $> 3\sigma$) and with c (with a correlation coefficient of 0.50 for SNe with $c < 0.5$, though the significance of this correlation is only at the $\sim 2\sigma$ level). One of these correlations is marginal; however, this spectral region has been studied very little in the past. A strength of the BSNIP data is that the average wavelength coverage (3300–10,400 Å, BSNIP I) is significantly wider than that of most other SN Ia spectral datasets. For example, one of the largest previously published SN Ia spectral datasets had an average wavelength coverage of 3700–7400 Å (Matheson et al. 2008).

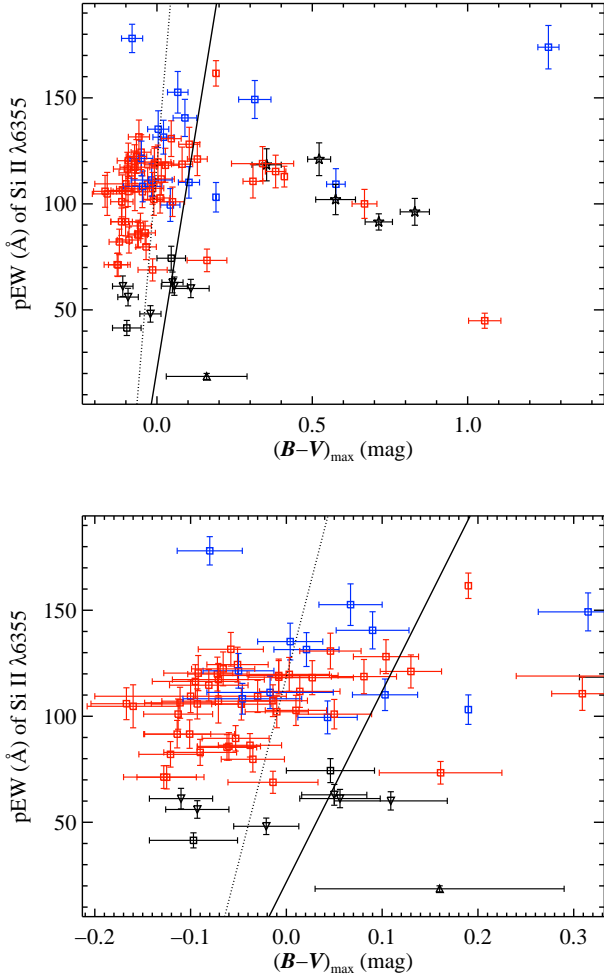


Figure 19. The pEW of the Si II $\lambda 6355$ feature versus $(B - V)_{\max}$ (*top*) and a close-up view of objects with $(B - V)_{\max} < 0.319$ mag (*bottom*). Colours and shapes of data points are the same as in Figure 5. The solid line is the fit to all of the data while the dotted line is the fit only to objects with $(B - V)_{\max} < 0.319$ mag.

Thus, the Ca II H&K feature, the O I triplet, and the Ca II near-IR triplet have been ignored almost entirely in past spectral analyses like the one presented here.

We once again constructed Hubble diagrams from Equations 4–7 and using the pEW values of Ca II H&K, the O I triplet, and the Ca II near-IR triplet. All but two models were significantly worse at measuring distances than the standard (x_1, c) model. The $(x_1, c, \text{Ca II H\&K pEW})$ and $(x_1, c, \text{O I triplet pEW})$ models both slightly decreased the WRMS, but at almost imperceptible levels ($\Delta_{x_1, c} = -0.0023 \pm 0.0096$ and $\Delta_{x_1, c} = -0.0063 \pm 0.0148$, respectively).

4.5 The Si II Ratio

Historically, one of the first spectral luminosity indicators investigated was the Si II ratio, $\mathfrak{R}(\text{Si II})$, defined by Nugent et al. (1995) as the ratio of the depth of the Si II $\lambda 5972$ feature to the depth of the Si II $\lambda 6355$ feature. Hachinger

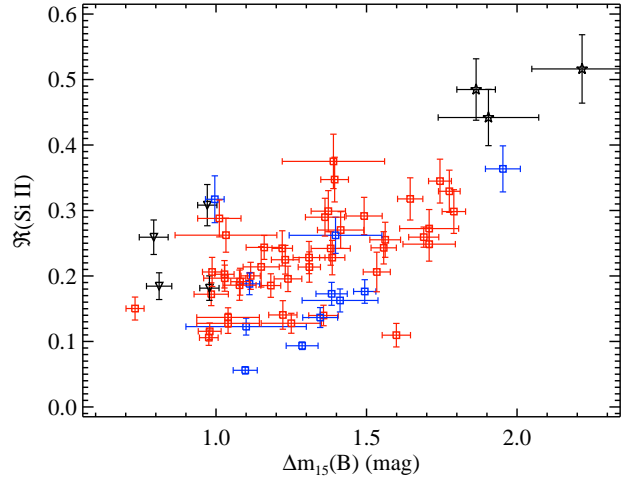


Figure 20. The Si II ratio versus $\Delta m_{15}(B)$. Colours and shapes of data points are the same as in Figure 5.

et al. (2006) redefined the Si II ratio as the pEW of Si II $\lambda 5972$ divided by the pEW of Si II $\lambda 6355$. In BSNIP II it was shown that these are nearly equivalent definitions, so in order to be consistent with that work we define the Si II ratio for the present study to be

$$\mathfrak{R}(\text{Si II}) \equiv \frac{\text{pEW}(\text{Si II } \lambda 5972)}{\text{pEW}(\text{Si II } \lambda 6355)}. \quad (12)$$

The Si II ratio has been shown to correlate with maximum absolute B -band magnitude and $\Delta m_{15}(B)$, which is why it has been used as a spectral luminosity indicator (e.g., Nugent et al. 1995; Benetti et al. 2005; Hachinger et al. 2006). Figure 20 shows 62 SNe Ia with both $\Delta m_{15}(B)$ and $\mathfrak{R}(\text{Si II})$. The data are correlated with a correlation coefficient of 0.62, which is significant at the $> 3\sigma$ level. Ia-91bg objects appear at the upper right of the plot and form a continuous relationship with the Ia-norm objects. Ia-99aa objects appear to lie above the main trend (though there are only a handful of these SNe in the figure), while HV objects lie below the main trend. When removing the Ia-99aa objects, the correlation increases slightly.

If we instead tag each data point in Figure 20 by its Benetti type, we find that the FAINT objects are found in the upper right of the main trend (similar to the Ia-91bg objects and as seen in previous studies, e.g., Benetti et al. 2005; Hachinger et al. 2006). The LVG and HVG objects are found in the lower-left portion of the plot with a significant level of overlap between the two subclasses. This differs from previous work, where there have been claims that LVG objects have larger Si II ratios and lie above the main trend (Benetti et al. 2005; Hachinger et al. 2006), though these studies and the BSNIP data both observe larger scatter in $\mathfrak{R}(\text{Si II})$ values in the lower $\Delta m_{15}(B)$ objects. When removing the LVG objects, the correlation is effectively unchanged. Comparing $\mathfrak{R}(\text{Si II})$ to the MLCS2k2 Δ parameter yields results similar to those seen in Figure 20.

The BSNIP distribution of $\Delta m_{15}(B)$ values, while not evenly distributed, is more continuous than in previous studies similar to the present one. For example, the data in Hachinger et al. (2006) contained only one object with

$\Delta m_{15}(B)$ between 1.5 and 1.7 mag, while the BSNIP data have 6 objects in that range. A more continuous distribution of $\Delta m_{15}(B)$ values, combined with the spectroscopic subclasses presented in Figure 20, complicates the relatively simplistic view that underpins the basic Phillips relation. For $0.95 \lesssim \Delta m_{15}(B) \lesssim 1.0$ mag there are Ia-99aa, Ia-norm, and HV objects. On the other end of the $\Delta m_{15}(B)$ distribution, between ~ 1.75 and ~ 1.95 mag there are Ia-91bg, Ia-norm, and again HV objects. Thus, for a given light-curve width (or decline rate), there exist SNe Ia of significantly different subclasses.

As discussed in BSNIP II, objects tagged by SNID as Ia-91bg or Ia-99aa are the most spectroscopically peculiar objects and probably only represent the extreme ends of a continuous distribution of spectra. If true, this means that the most spectroscopically peculiar objects *may not* have the most extreme light curves. The reverse may also be true, namely that the SNe with the most extreme light curves may not be the most spectroscopically peculiar. This is further supported by the relatively wide scatter in the main trend of Figure 20. At any value of $\Delta m_{15}(B)$ (with a significant number of objects) there is a broad range in $\mathfrak{R}(\text{Si II})$ values.

In BSNIP II, it was pointed out that the relative strength of the two Si II features that go into calculating $\mathfrak{R}(\text{Si II})$ is fairly robust at differentiating between the various ‘‘SNID types’’ and ‘‘Wang types.’’ Thus, from a spectrum, either using SNID or the pEWs of Si II features, one may declare an object to be Ia-91bg or Ia-99aa, whereas based on the light curve of the same object it might be considered relatively normal. The significant amount of scatter in the correlation between the Si II ratio and $\Delta m_{15}(B)$ also cautions one against simply measuring $\mathfrak{R}(\text{Si II})$ from a single spectrum and then using that value and a fit to the data in Figure 20 to calculate a $\Delta m_{15}(B)$ value.

In Figure 21 we show the 51 BSNIP SNe which have SALT2 fits and Si II ratios within 5 d of maximum brightness. $\mathfrak{R}(\text{Si II})$ is plotted against x_1 , c , and Hubble residuals corrected for colour only (for SNe which are used in the Hubble diagram).

From the BSNIP data we find that the Si II ratio is only marginally correlated with x_1 (top plot of Figure 21) with a correlation coefficient of -0.40 and significance of $\sim 2\sigma$. This is a weaker relationship than what has been found before (Blondin et al. 2011). The Ia-99aa objects appear to be above the main trend and most of the HV objects seem to be below it. The middle plot of Figure 21 shows no evidence for a correlation between $\mathfrak{R}(\text{Si II})$ and c , with a correlation coefficient of 0.14 for objects with $c < 0.5$.

The bottom plot of Figure 21 shows a low-significance correlation between the Si II ratio and Hubble residuals corrected for colour only (coefficient of 0.34), and it is again significantly weaker than what has been found before (Blondin et al. 2011). In fact, Blondin et al. (2011) go so far as to say that $\mathfrak{R}(\text{Si II})$ acts as a replacement for x_1 , but the BSNIP data do not support such a claim. Using the current sample, the best model which includes the Si II ratio also includes both x_1 and c , but it is only about as accurate as the standard (x_1, c) model ($\Delta_{x_1, c} = 0.0156 \pm 0.0114$).

Interestingly, Blondin et al. (2011) found that the sub-luminous (but Ia-norm) SN 2000k is a 2σ outlier in their plot of $\mathfrak{R}(\text{Si II})$ versus c , but part of the main correlation of $\mathfrak{R}(\text{Si II})$ versus x_1 . This object is in the BSNIP dataset and,

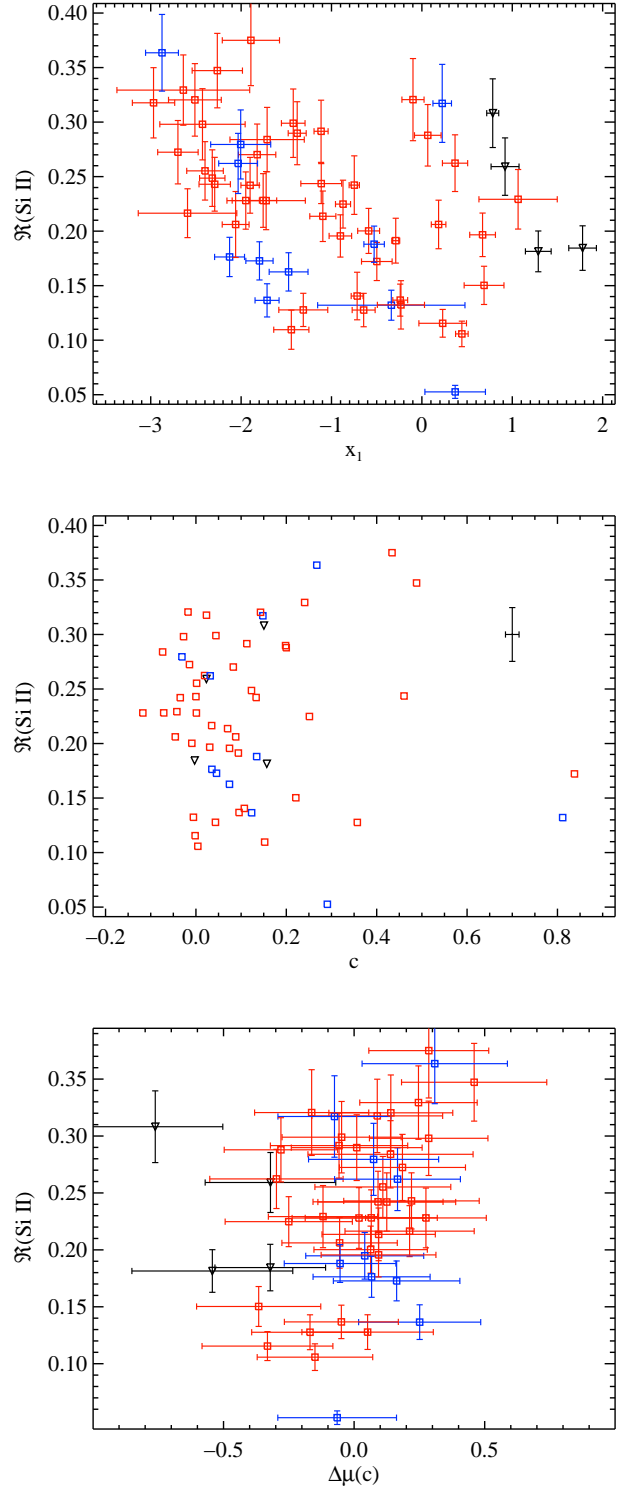


Figure 21. The Si II ratio versus SALT2 light-curve width parameter x_1 (top), SALT2 colour parameter c (middle), and Hubble residuals corrected for colour only (bottom). Colours and shapes of data points are the same as in Figure 5. In the middle plot, the median uncertainty in both directions is shown in the upper-right corner.

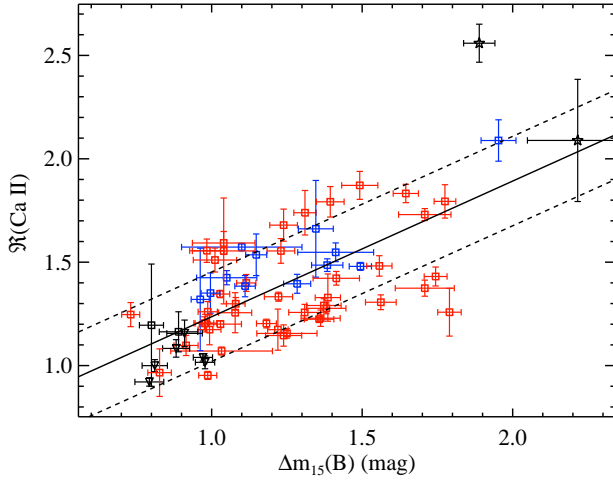


Figure 22. The Ca II ratio versus $\Delta m_{15}(B)$. Colours and shapes of data points are the same as in Figure 5. The solid line is the linear least-squares fit and the dashed lines are the standard error of the fit.

while we agree that it is subluminal and spectroscopically normal, it is not a significant outlier in any of the three plots in Figure 21.

4.6 The Ca II Ratio

The Ca II ratio was defined by Nugent et al. (1995) as the ratio of the flux at the red edge of the Ca II H&K feature to the flux at the blue edge of that feature. In the notation from BSNIP II this is

$$\mathfrak{R}(\text{Ca II}) \equiv \frac{F_r(\text{Ca II H\&K})}{F_b(\text{Ca II H\&K})}. \quad (13)$$

Like the Si II ratio, it has been found to correlate with maximum absolute B -band magnitude (Nugent et al. 1995).

In BSNIP II it was shown that the Ca II ratio and the Si II ratio are uncorrelated, even though both of them have been used as spectral luminosity indicators. In Section 4.5 it was shown that $\mathfrak{R}(\text{Si II})$ is correlated with $\Delta m_{15}(B)$. Figure 22 illustrates that $\mathfrak{R}(\text{Ca II})$ is correlated with $\Delta m_{15}(B)$ as well (correlation coefficient 0.70, significance $> 3\sigma$). The plot contains 65 SNe; the least-squares linear fit to the data is shown as the solid line in Figure 22, and the dashed lines are the standard error.

Interestingly, the HV objects seem to occupy a relatively narrow region of parameter space that is surrounded on all sides by mainly Ia-norm SNe. Ia-99aa objects mostly make up the lowest end of the linear trend, while one of the two Ia-91bg objects in the plot perhaps does not follow the main relationship. Unsurprisingly, comparing Δ to $\mathfrak{R}(\text{Ca II})$ results in the same trends seen in Figure 22.

Figure 23 displays the 64 BSNIP SNe which have SALT2 fits as well as Ca II ratios within 5 d of maximum brightness. $\mathfrak{R}(\text{Ca II})$ is plotted against x_1 , c , and Hubble residuals corrected for light-curve width and colour (for objects used when constructing the Hubble diagram).

The Ca II ratio appears to be well anticorrelated with x_1 (correlation coefficient -0.53 with significance $> 3\sigma$) and

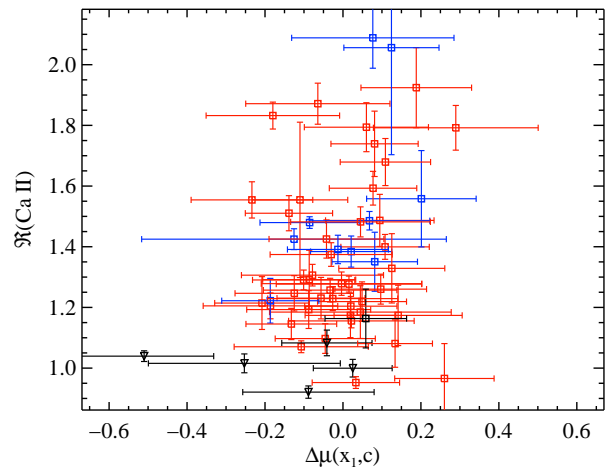
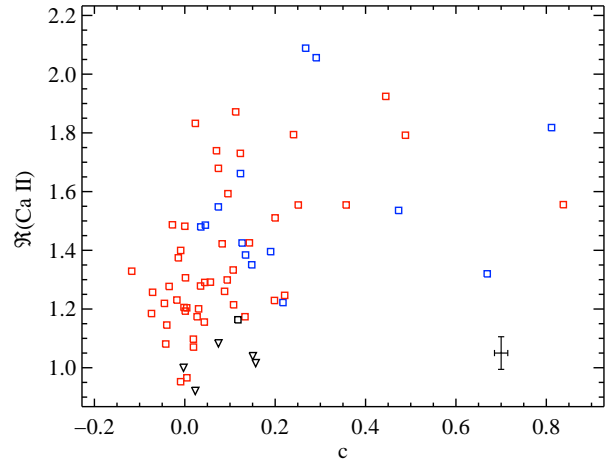
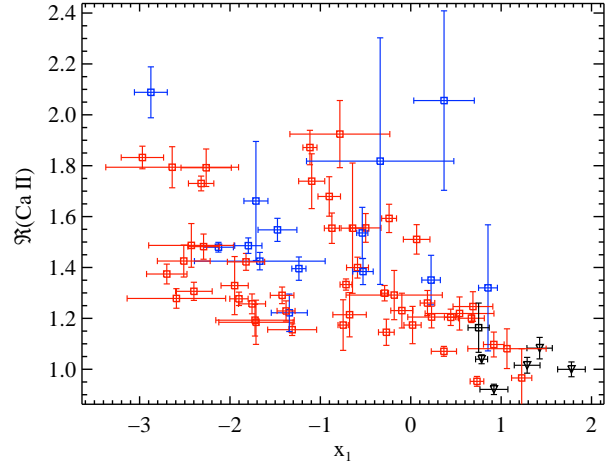


Figure 23. The Ca II ratio versus SALT2 light-curve width parameter x_1 (top), SALT2 colour parameter c (middle), and Hubble residuals corrected for light-curve width and colour (bottom). Colours and shapes of data points are the same as in Figure 5. In the middle plot, the median uncertainty in both directions is shown in the lower-right corner.

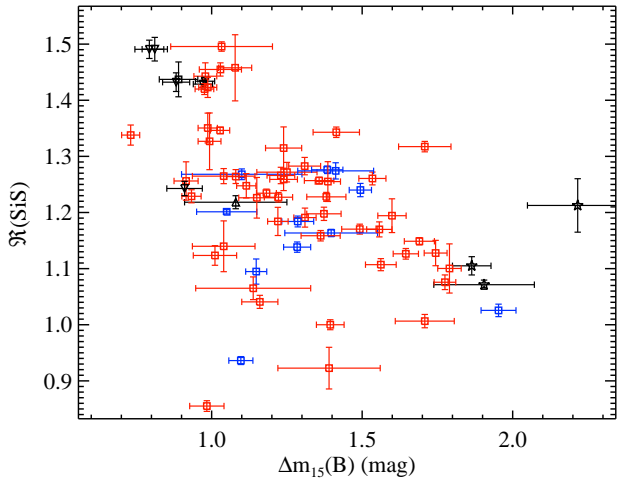


Figure 24. The SiS ratio versus $\Delta m_{15}(B)$. Colours and shapes of data points are the same as in Figure 5. The correlation coefficient is -0.54 .

correlated with c (coefficient of 0.46, again with significance $> 3\sigma$). The bottom plot of Figure 23 shows that the x_1 and c corrected Hubble residuals and $\mathfrak{R}(\text{Ca II})$ are not well correlated with each other (coefficient of 0.24). However, a model that uses x_1 , c , and the Ca II ratio decreases the WRMS by ~ 6 per cent and the σ_{pred} by ~ 33 per cent, although the significance of this improvement is only at the 1.1σ level ($\Delta_{x_1,c} = -0.0207 \pm 0.0191$).

4.7 The “SiS” Ratio

Analogous to the Ca II ratio, the “SiS ratio” was introduced by Bongard et al. (2006) as the ratio of the flux at the red edge of the S II “W” feature to the flux at the red edge of the Si II $\lambda 6355$ feature. In the notation used in BSNIP II this is

$$\mathfrak{R}(\text{SiS}) \equiv \frac{F_r(\text{S II “W”})}{F_r(\text{Si II } \lambda 6355)}. \quad (14)$$

In a sample of 8 SNe, $\mathfrak{R}(\text{SiS})$ has been seen to correlate with maximum absolute B -band magnitude in the same way as $\mathfrak{R}(\text{Ca II})$ (Bongard et al. 2006).

The SiS ratio and the Si II ratio were found to be only marginally correlated in BSNIP II, and Figure 24 (which contains 72 SNe) shows that $\mathfrak{R}(\text{SiS})$ is anticorrelated with $\Delta m_{15}(B)$ (correlation coefficient -0.50 and significance $\sim 3\sigma$). Note that this relationship is in the opposite sense of the one between the Ca II ratio and $\Delta m_{15}(B)$. Here Ia-99aa/91T objects lie above the main relationship while the Ia-norm and HV SNe are well mixed. Once again, comparing Δ or x_1 to $\mathfrak{R}(\text{SiS})$ yields similar results to what is seen in Figure 24.

The SiS ratio appears to be well correlated with c , when including the most reddened objects. In Figure 25 are 71 SNe, and the correlation coefficient is -0.61 (significant at the $> 3\sigma$ level). However, if one removes the most highly reddened objects with $c > 0.5$, the correlation weakens slightly to -0.56 (still with significance $> 3\sigma$). No distance model involving the SiS ratio is more accurate than the (x_1, c) model.

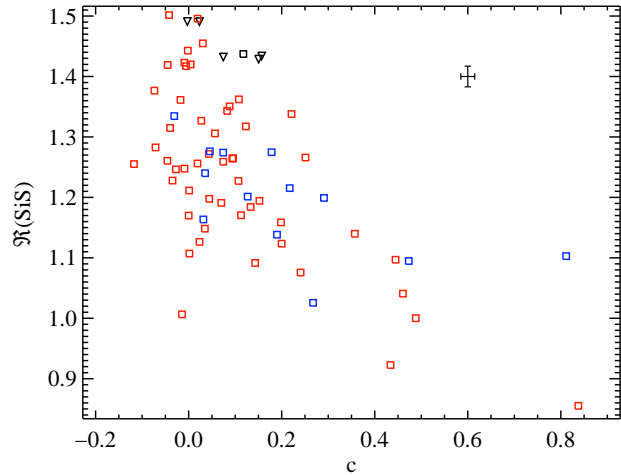


Figure 25. The SiS ratio versus c . Colours and shapes of data points are the same as in Figure 5. The median uncertainty in both directions is shown in the upper-right corner.

However, when $\mathfrak{R}(\text{SiS})$ is combined with just c or both x_1 and c , the accuracy is on par with the standard (x_1, c) model ($\Delta_{x_1,c} = 0.0209 \pm 0.0223$ and $\Delta_{x_1,c} = 0.0074 \pm 0.0105$, respectively). We also find (in Section 4.10) that out of 17,822 flux ratios combined with c , the most accurate distances are calculated using flux ratios that are effectively the SiS ratio, and that it is nearly as accurate as using the standard (x_1, c) model. Finally, we note that Blondin et al. (2011) found that $\mathfrak{R}(\text{SiS})$ performs significantly worse than the usual (x_1, c) model.

4.8 The “SSi” Ratio

Yet another possible spectroscopic luminosity indicator is the ratio of the pEW of the S II “W” to that of the Si II $\lambda 5972$ feature (Hachinger et al. 2006). This SSi ratio is defined in BSNIP II as

$$\mathfrak{R}(\text{S,Si}) \equiv \frac{\text{pEW}(\text{S II “W”})}{\text{pEW}(\text{Si II } \lambda 5972)}. \quad (15)$$

Hachinger et al. (2006) found that the SSi ratio is linearly anticorrelated with Δm_{15} (which is opposite to the relationship between $\mathfrak{R}(\text{Si II})$ and Δm_{15}). The analysis in BSNIP II seemed to confirm this observation by showing that the SSi ratio was strongly anticorrelated (nonlinearly) with the Si II ratio.

$\mathfrak{R}(\text{S,Si})$ is plotted against $\Delta m_{15}(B)$ for 59 SNe in Figure 26. The results of Hachinger et al. (2006) and the speculation in BSNIP II are confirmed: the SSi ratio is strongly anticorrelated with $\Delta m_{15}(B)$ (correlation coefficient of -0.67 with significance $> 3\sigma$). Here, the Ia-91bg and Ia-99aa objects follow the main trend and are found at the lower and upper ends of the correlation, respectively. There are only a few HV objects in Figure 26, but there is some evidence that they have larger than average $\mathfrak{R}(\text{S,Si})$ values (which was also seen in Fig. 16 of BSNIP II).

Plots of Δ and x_1 versus $\mathfrak{R}(\text{S,Si})$ display trends like that of Figure 26. However, the Ia-99aa objects fall off of the main correlation in both of these parameter spaces. In both cases

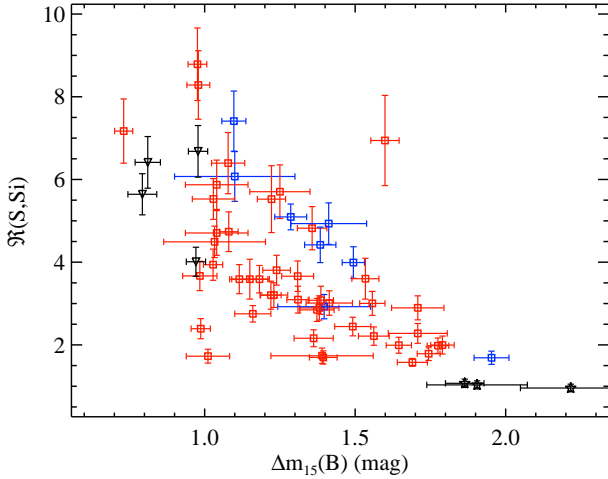


Figure 26. The SiSi ratio versus $\Delta m_{15}(B)$. Colours and shapes of data points are the same as in Figure 5.

these SNe have lower $\mathfrak{R}(\text{Si, Si})$ values than one would expect from the main correlation.

4.9 The “SiFe” Ratio

Analogous to the SiSi ratio, the “SiFe ratio” was defined as the ratio of the pEW of the Si II $\lambda 5972$ feature to that of the Fe II complex, and it was shown to be an accurate spectroscopic luminosity indicator (Hachinger et al. 2006). In BSNIP II, $\mathfrak{R}(\text{Si, Fe})$ was defined as

$$\mathfrak{R}(\text{Si, Fe}) \equiv \frac{\text{pEW}(\text{Si II } \lambda 5972)}{\text{pEW}(\text{Fe II})}, \quad (16)$$

and found to be strongly correlated with the Si II ratio.

We plot $\mathfrak{R}(\text{Si, Fe})$ versus $\Delta m_{15}(B)$ for 53 SNe in Figure 27. The results of Hachinger et al. (2006) and the speculation in BSNIP II are again confirmed: the SiFe ratio is strongly (linearly) correlated with $\Delta m_{15}(B)$, with a correlation coefficient of 0.68 (and with significance $> 3\sigma$). The solid line in the figure is the linear least-squares fit and the dashed lines are the standard error of the fit.

Similar to $\mathfrak{R}(\text{Si II})$, Ia-99aa objects are found at the lowest end of the linear trend while the Ia-91bg objects in the plot appear to be above the main relationship. In Figure 27 there are only a few HV SNe, but they appear to have smaller than average $\mathfrak{R}(\text{Si, Fe})$ values (which was also seen in Fig. 17 of BSNIP II). When comparing Δ and x_1 to $\mathfrak{R}(\text{Si, Fe})$, the basic trend seen in Figure 27 is recovered, but with larger scatter (even though the correlation coefficients are similar).

4.10 Arbitrary Flux Ratios

Bailey et al. (2009) found that by using ratios of fluxes from a single, binned SN Ia spectrum they could decrease the scatter in their Hubble diagrams. These ratios are defined as $\mathcal{R}(\lambda_y/\lambda_x) \equiv F(\lambda_y)/F(\lambda_x)$, where λ_y and λ_x are the rest-frame central wavelengths of given bins.⁵ The spectra are

⁵ This is similar to the definition of Bailey et al. (2009), but

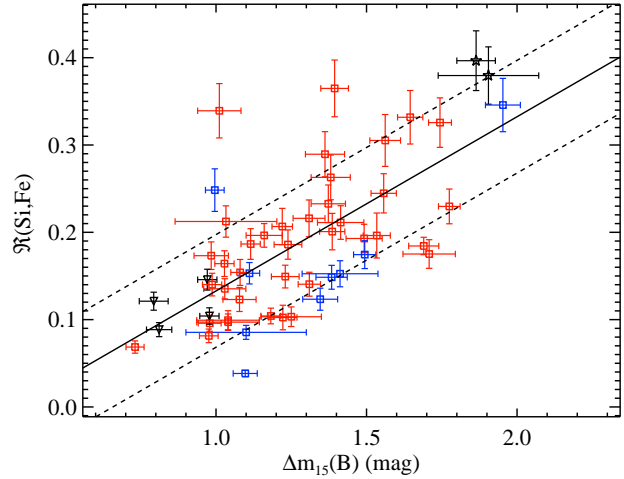


Figure 27. The SiFe ratio versus $\Delta m_{15}(B)$. Colours and shapes of data points are the same as in Figure 5. The solid line is the linear least-squares fit and the dashed lines are the standard error of the fit.

forced to cover a wavelength range of exactly 3500–8500 Å and are binned into 134 equal-sized (in $\ln \lambda$) bins (corresponding to 2000 km s⁻¹ per bin). The data are also deredshifted and dereddened using the redshift and reddening values presented in Table 1 of BSNIP I and assuming that the extinction follows the Cardelli et al. (1989) extinction law modified by O’Donnell (1994). As in Bailey et al. (2009) and Blondin et al. (2011), a colour-corrected version of this flux ratio ($\mathcal{R}^c(\lambda_y/\lambda_x)$) is also used, and it is defined as the ratio of fluxes as measured from a spectrum that has been corrected for SALT2 c using the colour law from Guy et al. (2007). We use these colour-corrected flux ratios when testing models that also adopt the SALT2 colour parameter (i.e., Equations 6 and 7).

As with the rest of the current study, we only investigate spectra within 5 d of maximum brightness since it was shown in BSNIP II that the spectra do not evolve significantly during these epochs. Also, as mentioned above, we do not use only spectra within 2.5 d of maximum (as has been done previously, Bailey et al. 2009; Blondin et al. 2011) because the significance of our results would be weakened due to the smaller number of objects. Since the average spectrum in BSNIP extends to 3300 Å (BSNIP I), we perform the current flux-ratio analysis with the requirement that all spectra cover a wavelength range of 3300–8500 Å. No ratios involving wavelengths below 3500 Å are found to decrease the WRMS significantly. We also vary the binning of the spectra used in the flux-ratio analysis and investigate data with bin sizes of 4000, 8000, and 10,000 km s⁻¹. We find that as the spectra are binned more, the WRMS values increase for all ratios. This can be explained by the idea that

is the reciprocal of the definition used by Blondin et al. (2011). However, this only really matters for the plots of λ_y versus λ_x in Figure 29. Thus, each panel in Figure 7 of Blondin et al. (2011) is the transpose of the panels in Figure 29. When using either definition, note that the first wavelength listed for a given \mathcal{R} is the numerator in the actual ratio of fluxes.

larger bins will “blend” wavelength bins of flux ratios that decrease the Hubble residuals with ones that do not and will thus add “noise” into flux ratios.

Since we are utilising SALT2 fits and Hubble diagrams, we again require that SNe have $z_{\text{helio}} > 0.01$, $c < 0.50$, and reduced $\chi^2 < 2$. Blondin et al. (2011) also require that the absolute difference between $B - V$ colour at maximum brightness derived from the spectrum and derived from the photometry be less than 0.1 mag. This is used as a proxy for their relative spectrophotometric accuracy. In BSNIP I it was shown (in Table 3) that the relative spectrophotometric accuracy is often < 0.1 mag for the BSNIP data. In fact, $B - V$ colour is only inaccurate at the 0.1 mag level for the oldest ($t > 20$ d) and noisiest ($S/N < 20$) BSNIP spectra. Therefore, the spectra investigated here should all be spectrophotometrically accurate enough for the flux-ratio analysis.

Of the data studied here, 62 objects have flux ratios calculated for the entire wavelength range mentioned above and reliable SALT2 fits that pass our Hubble diagram criteria (see Section 3.3). We randomly divide our sample into 9 groups of 7 SNe and 1 group with 6 SNe when doing 10-fold CV.

4.10.1 Flux-Ratio Results

The “best” flux ratios for each model are chosen to be the ones with the lowest WRMS values. Ranking by other parameters, such as the intrinsic prediction error (as used in Blondin et al. 2011), yields different values for the best-performing flux ratios. However, since our main goal is to minimise the scatter in the Hubble diagram, and since the WRMS has a relatively straightforward interpretation, we rank the best flux ratios by their WRMS values. As discussed in Section 3.3, for each model involving a flux ratio (Equations 4–7) we calculate, in addition to the WRMS, the intrinsic prediction error (σ_{pred}), the intrinsic correlation ($\rho_{x_1, c}$) of the residuals with residuals using the (x_1, c) model (Equation 8), and the difference ($\Delta_{x_1, c}$) in intrinsic prediction error with respect to the (x_1, c) model and its significance. These parameters, along with the wavelengths, of the top 10 ratios for each model which includes a flux ratio (Equations 4–7), are shown in Table 1.

Also displayed in Table 1 is the WRMS and σ_{pred} of our benchmark (x_1, c) model. Figure 28 shows the Hubble diagram residuals for this model versus redshift for the 62 SNe Ia mentioned above. The grey band indicates the WRMS for the model.

Figure 29 shows the WRMS (left column) and absolute Pearson correlation coefficient of the correction term (either $\gamma\mathcal{R}$ or $\gamma\mathcal{R}^c$) with the uncorrected Hubble residuals (right column) for all 17,822 ($= 134 \times 133$) flux ratios in all four models involving a flux ratio: \mathcal{R} , (x_1, \mathcal{R}) , (c, \mathcal{R}^c) , and (x_1, c, \mathcal{R}^c) (top to bottom, respectively). All ratios with WRMS values $\geq 2\sigma$ above the mean are displayed using the same colour.

The left column of Figure 29 is a proxy for the overall scatter in the model while the right column indicates how much “new” information is gained by adding in the correction term ($\gamma\mathcal{R}$ or $\gamma\mathcal{R}^c$). In general, a model may have a low WRMS (or σ_{pred}), meaning that the model is fitting the data well, but since the data have uncertainties associated with

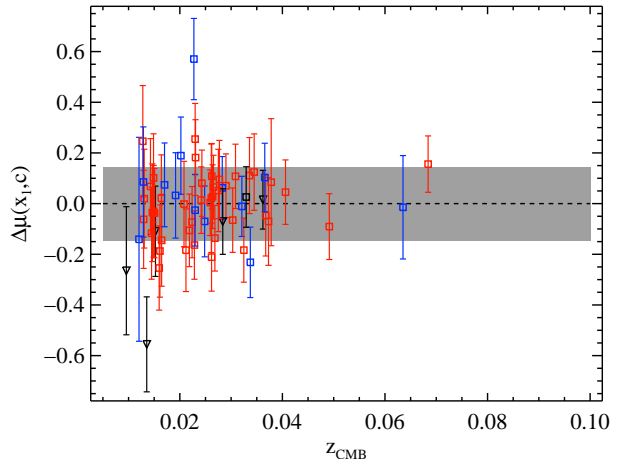


Figure 28. Hubble diagram residuals versus z_{CMB} for the standard (x_1, c) model (Equation 8). The grey band is the WRMS for the model. Colours and shapes of data points are the same as in Figure 5.

them, the model might be *overfitting* the data and actually end up fitting noise.

One way to discern whether this is the case is to see how well the correction terms correlate with the uncorrected Hubble residuals. As described in Section 4.2.2, if the terms that do not contain x_c or c (i.e., $\gamma\mathcal{R}$ or $\gamma\mathcal{R}^c$) are well correlated with the uncorrected Hubble residuals, then the measured observable is fitting information that actually exists in the data (as opposed to noise). However, a large correlation does not necessarily imply a good model. This is obvious (for example) in the top row of Figure 29, where most flux ratios have large WRMS values, including ones that also have quite high correlations between the correction term and the uncorrected Hubble residuals.

4.10.2 Model 1: \mathcal{R} Only

Using only a flux ratio (Equation 4) leads to no improvement over the usual (x_1, c) model (Equation 8). In fact, this model seems to perform significantly worse, as can be seen by the relatively large $\Delta_{x_1, c}$ values. The WRMS and σ_{pred} of the “best” ratios are quite a bit larger than those of the (x_1, c) model. This differs from the conclusion of previous work, which found that models using a flux ratio alone could perform as well as the (x_1, c) model (Bailey et al. 2009; Blondin et al. 2011). The best-performing ratio in the \mathcal{R} -only model, \mathcal{R} (7770/3750), is not correlated with x_1 , but is highly correlated with c (correlation coefficient 0.81). This implies that \mathcal{R} (7770/3750) is effectively a colour indicator.

The best ratio using this model seen by Blondin et al. (2011), \mathcal{R} (6630/4400), was found in their study to be similarly correlated with SALT2 colour and to improve the Hubble diagram residuals over using the (x_1, c) model (albeit with a low significance). We tested all of our flux-ratio models using a randomly selected subset of 26 SNe from the BSNIP sample in order to match the number of objects used by Blondin et al. (2011). These models all yielded WRMS values similar to what was found by Blondin et al.

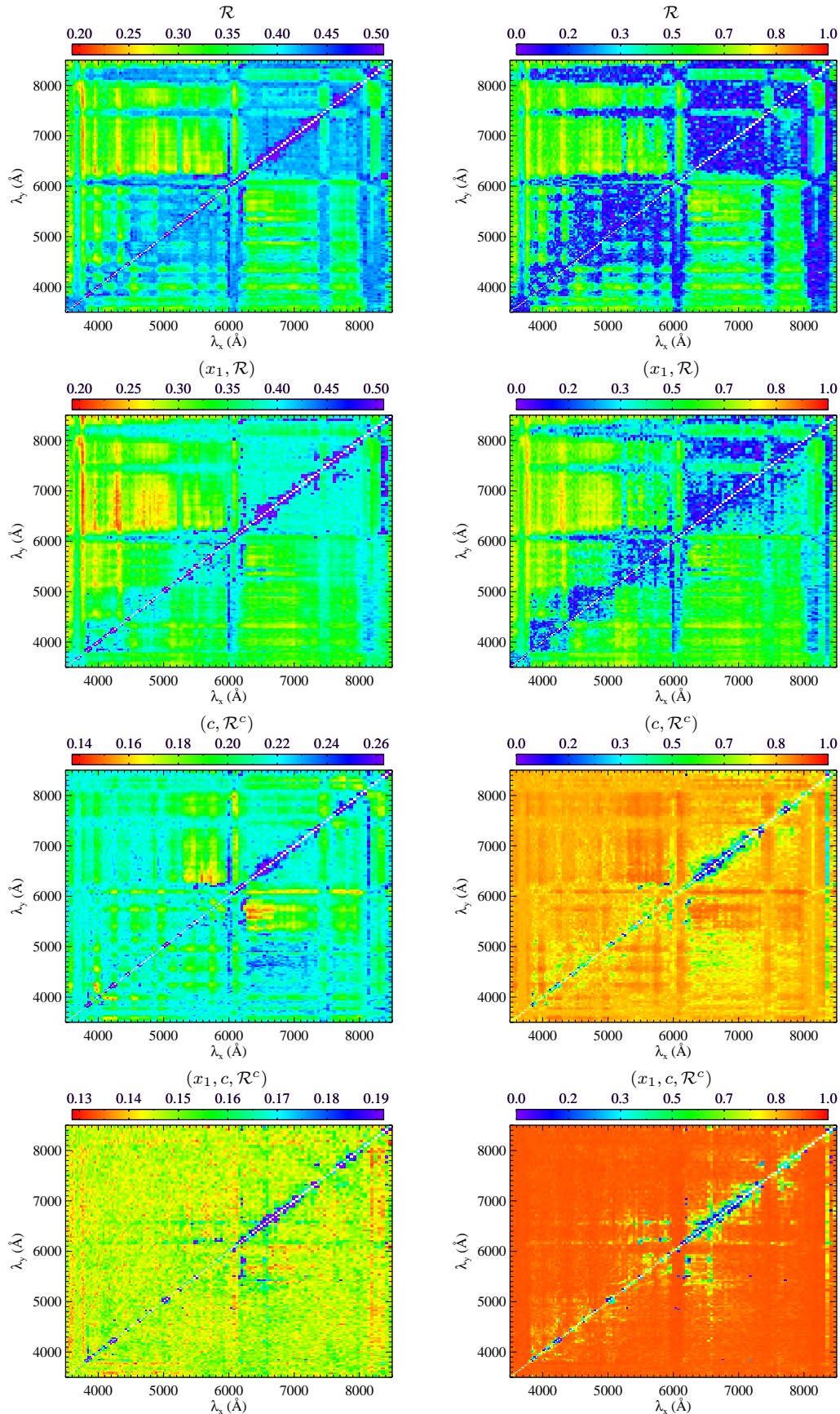


Figure 29. A map of the WRMS (*left column*) and the absolute Pearson correlation coefficient of the correction term with the uncorrected Hubble residuals (*right column*) for all 17,822 flux ratios used in all four models involving a flux ratio (\mathcal{R} only, (x_1, \mathcal{R}) , (c, \mathcal{R}^c) , and (x_1, c, \mathcal{R}^c) , *top to bottom*, respectively). All ratios with WRMS values $\geq 2\sigma$ above the mean have the same colour.

Table 1. Top 10 Flux Ratios for Each Model

Rank	λ_y	λ_x	WRMS (mag)	σ_{pred} (mag)	$\rho_{x_1, c}$	$\Delta_{x_1, c}$
\mathcal{R}						
1	7770	3750	0.218 ± 0.027	0.179 ± 0.023	-0.11	0.095 ± 0.030 (3.2σ)
2	7670	3750	0.223 ± 0.028	0.189 ± 0.023	0.09	0.104 ± 0.030 (3.5σ)
3	7720	3750	0.223 ± 0.027	0.188 ± 0.023	-0.05	0.103 ± 0.030 (3.4σ)
4	7930	3750	0.226 ± 0.030	0.187 ± 0.023	-0.10	0.104 ± 0.031 (3.4σ)
5	6990	3750	0.227 ± 0.030	0.193 ± 0.023	-0.17	0.111 ± 0.031 (3.6σ)
6	7880	3750	0.227 ± 0.027	0.190 ± 0.023	-0.06	0.106 ± 0.030 (3.5σ)
7	7670	3780	0.230 ± 0.030	0.199 ± 0.024	0.08	0.114 ± 0.030 (3.8σ)
8	6990	3780	0.231 ± 0.029	0.202 ± 0.023	-0.21	0.121 ± 0.031 (3.9σ)
9	6900	3750	0.233 ± 0.029	0.198 ± 0.024	-0.18	0.116 ± 0.031 (3.7σ)
10	7040	3780	0.234 ± 0.029	0.208 ± 0.023	-0.15	0.127 ± 0.031 (4.1σ)
(x_1, \mathcal{R})						
1	6990	3750	0.199 ± 0.022	0.160 ± 0.022	-0.19	0.080 ± 0.031 (2.6σ)
2	7770	3750	0.200 ± 0.024	0.160 ± 0.022	-0.09	0.077 ± 0.030 (2.6σ)
3	6720	3750	0.203 ± 0.024	0.166 ± 0.022	-0.28	0.088 ± 0.031 (2.8σ)
4	6900	3750	0.204 ± 0.024	0.164 ± 0.022	-0.18	0.083 ± 0.031 (2.7σ)
5	6760	3750	0.206 ± 0.027	0.165 ± 0.022	-0.22	0.085 ± 0.031 (2.8σ)
6	6950	3750	0.206 ± 0.024	0.166 ± 0.023	-0.19	0.085 ± 0.031 (2.7σ)
7	6850	3750	0.206 ± 0.024	0.166 ± 0.022	-0.22	0.085 ± 0.031 (2.8σ)
8	7930	3750	0.209 ± 0.027	0.167 ± 0.022	-0.12	0.085 ± 0.030 (2.8σ)
9	6590	3750	0.209 ± 0.028	0.166 ± 0.023	-0.23	0.092 ± 0.032 (2.9σ)
10	6990	3780	0.209 ± 0.027	0.177 ± 0.022	-0.19	0.097 ± 0.030 (3.2σ)
(c, \mathcal{R}^c)						
1	5580	6330	0.146 ± 0.021	0.083 ± 0.022	0.43	-0.004 ± 0.018 (0.2σ)
2	3980	4140	0.147 ± 0.017	0.076 ± 0.025	0.56	-0.002 ± 0.017 (0.1σ)
3	6330	5580	0.149 ± 0.021	0.086 ± 0.022	0.46	0.002 ± 0.018 (0.1σ)
4	5730	6370	0.149 ± 0.019	0.087 ± 0.022	0.41	0.002 ± 0.019 (0.1σ)
5	6370	5580	0.150 ± 0.019	0.094 ± 0.021	0.42	0.009 ± 0.018 (0.5σ)
6	5580	6290	0.150 ± 0.022	0.076 ± 0.025	0.39	-0.012 ± 0.021 (0.6σ)
7	5730	6330	0.150 ± 0.019	0.087 ± 0.023	0.43	-0.000 ± 0.019 (0.0σ)
8	5580	6420	0.151 ± 0.021	0.093 ± 0.021	0.43	0.003 ± 0.019 (0.2σ)
9	5690	6330	0.151 ± 0.021	0.085 ± 0.022	0.18	0.009 ± 0.022 (0.4σ)
10	6370	5730	0.151 ± 0.018	0.083 ± 0.024	0.64	-0.002 ± 0.019 (0.1σ)
(x_1, c, \mathcal{R}^c)						
1	3780	4580	0.130 ± 0.017	0.050 ± 0.029	0.81	-0.020 ± 0.012 (1.7σ)
2	3610	4890	0.132 ± 0.015	0.056 ± 0.028	0.71	-0.016 ± 0.014 (1.2σ)
3	5360	6900	0.132 ± 0.017	0.062 ± 0.025	0.84	-0.014 ± 0.010 (1.4σ)
4	4760	3800	0.132 ± 0.020	0.065 ± 0.025	0.84	-0.012 ± 0.010 (1.2σ)
5	7980	8140	0.133 ± 0.015	0.062 ± 0.025	0.69	-0.021 ± 0.015 (1.4σ)
6	7720	8200	0.133 ± 0.015	0.061 ± 0.026	0.94	-0.013 ± 0.008 (1.6σ)
7	6080	6210	0.133 ± 0.020	0.054 ± 0.029	0.79	-0.019 ± 0.013 (1.5σ)
8	3610	4170	0.133 ± 0.015	0.064 ± 0.025	0.81	-0.009 ± 0.010 (0.9σ)
9	4280	3780	0.133 ± 0.015	0.062 ± 0.026	0.80	-0.011 ± 0.011 (1.0σ)
10	3610	4230	0.133 ± 0.017	0.062 ± 0.024	0.73	-0.016 ± 0.013 (1.2σ)
(x_1, c)						
...	0.144 ± 0.019	0.076 ± 0.023

(2011), though the best-performing flux ratios were significantly different and the significance of the improvement was decreased (mostly due to the fact that the (x_1, c) model performed much worse when using only 26 objects). Much like our analysis which only used spectra within 2.5 d of maximum brightness, the decrease in sample size was chiefly responsible for the weakened significance of Hubble residual improvement.

Bailey et al. (2009) also saw an overall improvement when using their top ratio for this model, \mathcal{R} (6420/4430). The WRMS for both of these ratios using the BSNIP data is ~ 0.35 mag, which is much larger than the WRMS values seen for our best ratios. When the BSNIP data are fit using $K = 2$, the WRMS of the best-performing ratio does decrease as

compared to our $K = 10$ run. However, the best-performing ratios involve wavelengths that are randomly scattered in wavelength space which may imply that these results are less reliable than the more statistically rigorous run using $K = 10$.

4.10.3 Model 2: \mathcal{R} and x_1

Combining a flux ratio with the SALT2 stretch parameter x_1 (Equation 5) also leads to no improvement over the (x_1, c) model. The WRMS and σ_{pred} values are smaller than when using the \mathcal{R} -only model, but they are still significantly larger than those from the standard (x_1, c) model. We again point

out that Blondin et al. (2011) found that the (x_1, \mathcal{R}) model did better than the (x_1, c) model.

The best flux ratio using the (x_1, \mathcal{R}) model, $\mathcal{R}(6990/3750)$, is (like the \mathcal{R} -only model) not correlated with x_1 , but strongly correlated with c (coefficient of 0.83). The ratio $\mathcal{R}(6990/3750)$ is therefore a proxy for c , and so it is unsurprising that this is the top-ranked ratio in a model employing only a ratio and x_1 . Using this model Blondin et al. (2011) again found that the ratio $\mathcal{R}(6630/4400)$ was best and, as mentioned above, it was similarly correlated with SALT2 c . Nearly all of the top ten ratios for the \mathcal{R} -only and (x_1, \mathcal{R}) models have very similar numerator and denominator wavelengths, and the difference in wavelength between the two fluxes is significant (3000–4000 Å). This again supports the idea presented above that the top-ranked flux ratios for these two models are effectively proxies for colour.

4.10.4 Model 3: \mathcal{R}^c and c

Some of the top-ranked flux ratios with the SALT2 colour parameter c (Equation 6) are consistent with the results when using the (x_1, c) model. This lack of improvement is once again at odds with what was seen by Blondin et al. (2011). However, as mentioned in Section 4.10.2, the apparent improvement in Blondin et al. (2011) is likely due to their smaller sample size and the relatively poor performance of the (x_1, c) model.

Many ratios appear to have large correlations between the correction terms and uncorrected residuals, but the lowest WRMS values are tightly clustered in wavelength space. This is also apparent in Table 1, where all but one of the top ten ratios for the (c, \mathcal{R}^c) model involve wavelengths near 5600 Å and 6300 Å. Flux ratios which include these wavelengths are effectively the same as $\mathfrak{R}(\text{SiS})$, the SiS ratio (Section 4.7).

The SiS ratio was shown above to be anticorrelated with $\Delta m_{15}(B)$ (as well as correlated with x_1). The best flux ratio using the (c, \mathcal{R}^c) model, $\mathcal{R}^c(5580/6330)$, is strongly correlated with x_1 (correlation coefficient 0.83) and effectively uncorrelated with c (correlation coefficient -0.18). Therefore, the top-ranked ratio for this model can be thought of as equivalent to $\mathfrak{R}(\text{SiS})$ and/or x_1 . Furthermore, the lack of correlation between $\mathcal{R}^c(5580/6330)$ and c implies that dereddening the data using the SALT2 c and colour law is working as intended.

With the (c, \mathcal{R}^c) model, Blondin et al. (2011) showed that their top-ranked ratio was $\mathcal{R}^c(6420/5290)$. This is similar to the reciprocal of the best ratio found with the BSNIP data; thus, it is not surprising that they find a strong *anticorrelation* between $\mathcal{R}^c(6420/5290)$ and x_1 . Their ratio also leads to a larger decrease in WRMS (~ 15 per cent, Blondin et al. 2011). Bailey et al. (2009) again showed an improvement when using their top ratio for this model, $\mathcal{R}^c(6420/5190)$, which is also very close to the best ratio of Blondin et al. (2011), as well as the reciprocal of the best ratio presented here. Despite this similarity in wavelength space, the top-ranked ratios for this model from Bailey et al. (2009) and Blondin et al. (2011) yield WRMS values of ~ 0.21 mag when using the BSNIP data.

4.10.5 Model 4: \mathcal{R}^c , x_1 , and c

Quite significant improvements over the standard (x_1, c) model are seen when using the top-ranked flux ratios along with both x_1 and c (Equation 7). In fact, the top ten ratios lead to improvements at about the $1-2\sigma$ level (see Table 1). Furthermore, a good fraction of the ratios lead to some improvement over the standard model. Figure 30 shows a histogram of the WRMS values for the (x_1, c, \mathcal{R}^c) model (solid line) and the expected Gaussian distribution (dotted line). The short-dashed and long-dashed lines are the peak of the WRMS distribution and the WRMS value of the standard (x_1, c) model, respectively. The distribution is roughly Gaussian when one ignores the high-WRMS tail (i.e., $\text{WRMS} \gtrsim 0.17$, or ratios with WRMS values that are $> 5\sigma$ away from the peak of the distribution). The bottom panel of Figure 30 shows a close-up view of the smallest WRMS values. The fact that the best performing flux ratios (i.e., the ones yielding the smallest WRMS values) lie quite a bit above the Gaussian expectation seems to indicate that these are in fact statistically significant decreases in the WRMS, as indicated by the last column of Table 1.

The (x_1, c, \mathcal{R}^c) model and its best ratio, $\mathcal{R}^c(3780/4580)$, decrease the WRMS by ~ 10 per cent and σ_{pred} by ~ 34 per cent from the (x_1, c) model. The Hubble diagram for the top-ranked flux ratio using the (x_1, c, \mathcal{R}^c) model is shown in Figure 31, along with the WRMS for the best model (the grey band).

The decrease in WRMS using this model is smaller than previously seen, but the decrease in σ_{pred} is larger and the overall improvement is at a higher significance; Blondin et al. (2011) found a 20 per cent decrease in WRMS with a 1.6σ significance. The fact that the current dataset has nearly three times as many objects as the sample studied by Blondin et al. (2011) is likely the reason why the (x_1, c, \mathcal{R}^c) model yields more significant improvements in WRMS values.

Most ratios have low values of WRMS and extremely large correlations between the correction terms and uncorrected residuals, implying that the (x_1, c, \mathcal{R}^c) model is performing better overall than any of the other models investigated. This is consistent with Blondin et al. (2011), although they found no flux ratio to have a strong correlation between the correction terms and the uncorrected Hubble residuals. The wavelengths of six of the top ten ratios for this model are near ~ 3750 Å and ~ 4550 Å with wavelength baselines of ~ 800 Å. These approximately correspond to the midpoint of the Ca II H&K feature and the border between the Mg II and Fe II complexes.

Figure 32 shows the best flux ratio using the (x_1, c, \mathcal{R}^c) model, $\mathcal{R}^c(3780/4580)$, versus the SALT2 parameters x_1 and c . There is a slight correlation of this ratio with x_1 (correlation coefficient 0.46) and effectively no correlation with c . Since this ratio is essentially uncorrelated with both SALT2 parameters and it decreases the WRMS at the $\sim 2\sigma$ level, it yields useful information about each SN beyond light-curve stretch and colour. It is intriguing that this new information is found at the blue end of the optical range, since there is evidence that spectral features in this region do not correlate with light-curve parameters, yet contain information related to SN Ia luminosity (e.g., Foley et al. 2008).

Note that Blondin et al. (2011) found that flux ratios

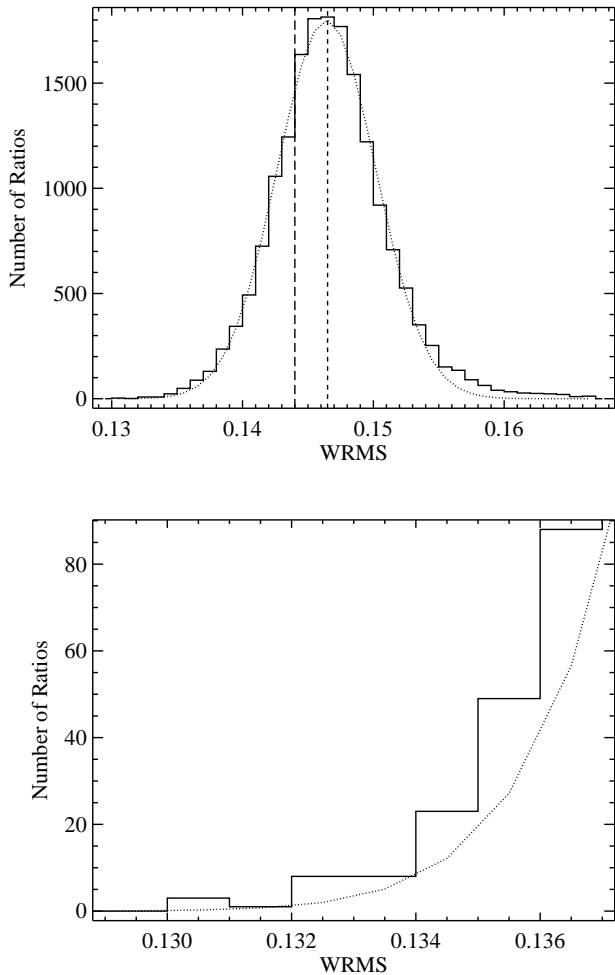


Figure 30. A histogram of the WRMS values for the (x_1, c, \mathcal{R}^c) model (solid line) and the expected Gaussian distribution (dotted line) for ratios with WRMS values that are $< 5\sigma$ away from the peak of the distribution (*top*). The short-dashed and long-dashed lines are the peak of the WRMS distribution and the WRMS value of the standard (x_1, c) model, respectively. A close-up view of the smallest WRMS values (*bottom*).

with wavelengths near $\sim 5300 \text{ \AA}$ and baselines of $< 400 \text{ \AA}$ gave the best results for the (x_1, c, \mathcal{R}^c) model. Using the best ratio from their study, \mathcal{R}^c (5690/5360), the BSNIP data yield a WRMS of ~ 0.15 mag, which is not as good as our top ten ratios.

5 CONCLUSIONS

This is the third paper in the BSNIP series and presents a comparison between spectral feature measurements and photometric properties of 108 low-redshift ($z < 0.1$) SNe Ia within 5 d of maximum brightness. The spectral data all come from BSNIP I, and the photometric data come mainly from the LOSS sample and are published by Ganeshalingam et al. (2010). The details of the spectral measurements can be found in BSNIP II, and the light-curve fits and photometric parameters are in Ganeshalingam et al. (in preparation). A combination of light-curve parameters (specifically

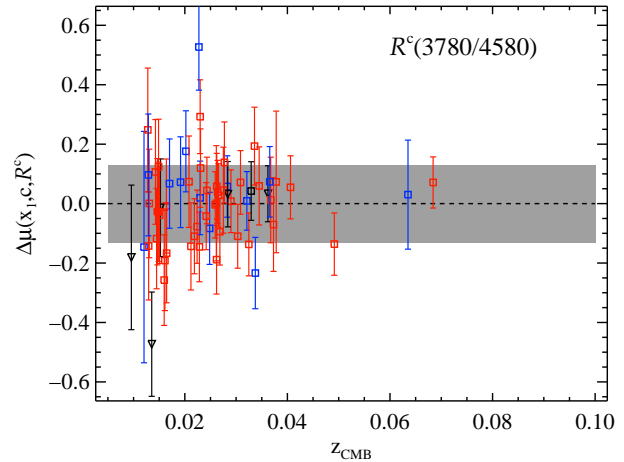


Figure 31. Hubble diagram residuals versus z_{CMB} for the best flux ratio, \mathcal{R}^c (3780/4580), using the (x_1, c, \mathcal{R}^c) model (Equation 7). The grey band is the WRMS for the model. Colours and shapes of data points are the same as in Figure 5.

the SALT2 stretch and colour parameters x_1 and c) and spectral measurements are used to calculate distances to SNe Ia. We then compare the residuals from these models to the standard model which only uses light-curve stretch and colour. Future BSNIP papers will incorporate host-galaxy properties and SN spectra at later epochs into the analysis presented here.

5.1 Summary of Investigated Correlations

The velocity gradient (Benetti et al. 2005) is compared to the light-curve width, and it is shown that, as in BSNIP II, the various classifications based on the value of \dot{v} overlap significantly. Similarly, velocities at maximum brightness (v_0) are compared to photometric observables and classifications based on velocity gradient, and there is a large amount of overlap in all of these parameters as well. In earlier work, HV and HVG objects have been used almost interchangeably, as have normal velocity and LVG objects (e.g., Hachinger et al. 2006; Pignata et al. 2008; Wang et al. 2009). However, the analyses of BSNIP II and this work show that these associations are not as distinct as previously thought.

The measured velocities of the Si II $\lambda 6355$ and Si II $\lambda 5972$ features near maximum brightness are uncorrelated with observed $(B - V)_{\text{max}}$. Furthermore, the HV objects and normal-velocity objects have similar distributions of observed $(B - V)_{\text{max}}$ values, though the HV objects tend to have slightly larger observed $(B - V)_{\text{max}}$. When distances to SNe Ia are computed using light-curve width (x_1) and colour (c) parameters, no significant improvement in the accuracy of the distances is found when the velocity of the Si II $\lambda 6355$ feature is added. This is contrary to what was seen by Blondin et al. (2011). Furthermore, models involving x_1 , c , and the velocity of the Ca II H&K feature fare as poorly. However, the velocity of the S II “W,” when used in conjunction with x_1 and c , leads to a decrease in the WRMS of the distances at the 1.8σ level. Despite what was seen in the analysis of Blondin et al. (2011), the use of relative depths of

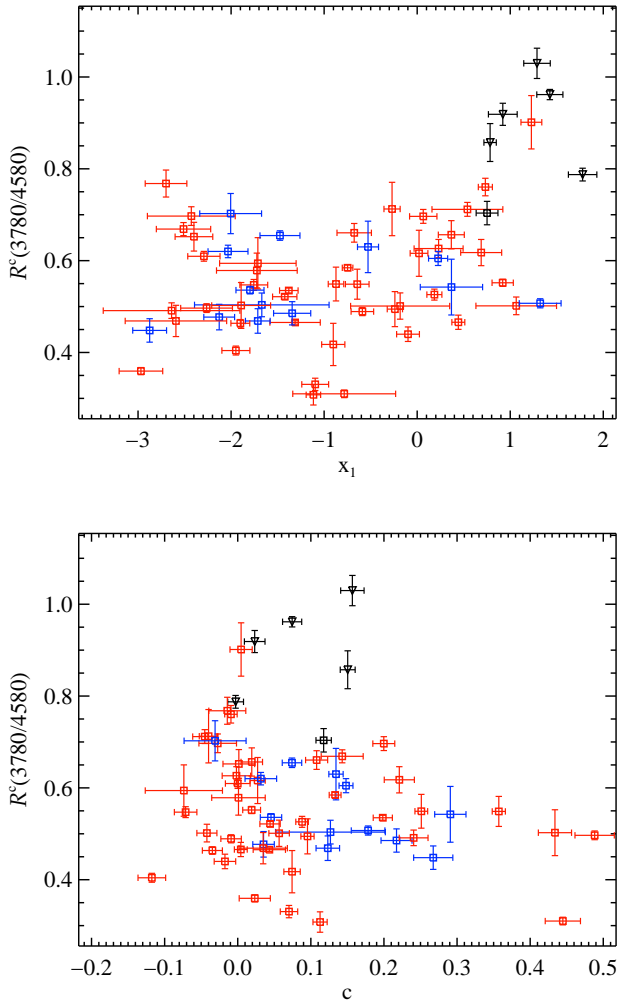


Figure 32. The top-ranked flux ratio, $\mathcal{R}^c(3780/4580)$, using the (x_1, c, \mathcal{R}^c) model (Equation 7) versus the SALT2 parameters x_1 and c . Colours and shapes of data points are the same as in Figure 5.

none of the features analysed here leads to an improvement in the Hubble residuals.

The pEW of the Si II $\lambda 4000$ feature is strongly anti-correlated with x_1 , which confirms many previous studies (Arsenijevic et al. 2008; Walker et al. 2011; Blondin et al. 2011; Nordin et al. 2011b; Chotard et al. 2011). Furthermore, when using a model that includes x_1 , c , and the pEW of this feature, the residuals are as low as when using the standard (x_1, c) model. The pEWs of the Mg II and Fe II complexes are both correlated with c , and since interstellar reddening cannot affect pEWs significantly, it seems that it is the *intrinsic* colour of the SN which is correlated with both of these pEWs. However, when using either of these pEWs (as a proxy for c) combined with the pEW of the Si II $\lambda 4000$ feature (as a proxy for x_1), the Hubble diagram residuals are significantly larger than when simply using x_1 and c .

The pEWs of both Si II $\lambda 5972$ and Si II $\lambda 6355$ are well correlated with x_1 and correlated with c , but the use of the Si II $\lambda 5972$ pEW does not improve distance calculations.

However, using the Si II $\lambda 6355$ pEW (along with x_1 and c) leads to an improvement in the WRMS residuals at the 1.2σ level. Finally, the Ca II near-IR triplet is correlated with c and MLCS2k2 light-curve width parameter Δ . This feature and the O I triplet have not been investigated thoroughly in studies similar to this one since other large SN Ia spectral datasets often do not include these spectral regions.

The Si II ratio, used as a luminosity indicator previously (e.g., Nugent et al. 1995; Benetti et al. 2005; Hachinger et al. 2006), is found to be well correlated with Δm_{15} . However, we caution that at a given value of Δm_{15} , there can exist various spectroscopically classified subtypes of SNe Ia. This ratio is also found to be correlated with observed $(B - V)_{\max}$, which has been seen in other work (Altavilla et al. 2009). We also show that the Si II ratio is *not* an accurate proxy for x_1 when calculating distance moduli. A model using c and $\mathcal{R}(\text{Si II})$ performs significantly worse than the usual (x_1, c) model, contrary to the conclusion of Blondin et al. (2011).

On the other hand, the Ca II ratio is found to be a good indicator of light-curve width, as it is well correlated with the MLCS2k2 Δ parameter and with Δm_{15} . The BSNIP data also indicate that the SiS ratio is correlated with both x_1 and c , and distance models using $\mathcal{R}(\text{SiS})$ with just c or with both c and x_1 perform as well as the standard (x_1, c) model. Finally, we confirm the results of Hachinger et al. (2006) that the SSi and SiFe ratios are both accurate luminosity indicators, as they are both well correlated with Δm_{15} .

Following Bailey et al. (2009) and Blondin et al. (2011), we calculate Hubble diagram residuals using models which include combinations of the usual light-curve parameters (width and colour) and arbitrary sets of flux ratios. A total of 17,822 different ratios of fluxes are used alone, with x_1 , with c , and with both x_1 and c to investigate whether any of these models might improve the accuracy of SN Ia distance measurements. No models utilising only a flux ratio or a flux ratio and x_1 are found to decrease the Hubble residuals. A handful of models using a flux ratio and c are seen to perform as well as the standard (x_1, c) model. Interestingly, most of these best ratios are extremely close to the SiS ratio mentioned above.

These results differ from those of the previous studies of Bailey et al. (2009) and Blondin et al. (2011), both of which found that flux ratios alone or in conjunction with light-curve information would usually perform better than the (x_1, c) model. This may be due to the fact that our “standard model” (without a spectral indicator) already performs significantly better than that of Bailey et al. (2009) or Blondin et al. (2011). The differences may also be caused by the larger number of spectroscopically peculiar SNe Ia in the BSNIP sample.

Finally, when combining a flux ratio with both x_1 and c , our top-performing ratio, $\mathcal{R}^c(3780/4580)$, decreases the Hubble residuals by 10 per cent, which is significant at the 2σ level. The WRMS of the residuals using this model is 0.130 ± 0.017 mag, as compared to 0.144 ± 0.019 mag when using the same sample with the standard (x_1, c) model. This Hubble diagram has one of the smallest scatters ever published and at the highest significance ever seen in such a study. The wavelengths involved in most of the best-performing ratios in the (x_1, c, \mathcal{R}^c) model approximately correspond to the midpoint of the Ca II H&K feature and the border between the Mg II and Fe II complexes. This sup-

ports previous work which has shown that near-UV spectra of SNe Ia contain information related to SN Ia luminosity which is not necessarily captured in the photometry (e.g., Foley et al. 2008).

5.2 The Future

New large-scale surveys are already obtaining SN Ia data, and they are observing to higher redshifts and gathering larger amounts of data than what is in the BSNIP sample (e.g., Rau et al. 2009; Law et al. 2009; Kaiser et al. 2002). Even larger surveys at even higher redshifts are also planned (e.g., LSST, WFIRST). Many more SNe Ia will be discovered than can be rigorously observed; we are quickly entering the age of SN research where we are limited by the follow-up observations. Thus, there must be significant effort put forth to determine the most efficient way to monitor and utilise such vast quantities of objects. That is one of the major goals of BSNIP.

Soon, for the vast majority of objects, there will only be (at best) a handful of photometric observations near maximum brightness. Those, combined with a relatively low S/N spectrum near maximum, will likely be all the follow-up observations we get. From the work presented here (and in BSNIP II) we have shown that there still is hope.

The pEW of the Si II $\lambda 4000$ feature is a good indicator of light-curve width, and the pEWs of the Mg II and Fe II complexes are relatively good proxies for colour. Unfortunately, the correlations between these spectral measurements and the corresponding photometric properties is not perfect, and distance calculations that employ only these spectroscopic measurements do not perform as well as the standard model which uses light-curve width and colour. However, this is still a promising avenue for further investigation using new datasets that are even larger than BSNIP. Other correlations that appear marginal in the BSNIP dataset, or models tested here that performed only equally as well as the usual (x_1, c) model, should also be reexamined in the future.

Occasionally, one will be fortunate enough to have sufficient photometric observations to produce a light curve for which SALT2 (or another light-curve fitter) is able to determine a width and colour. In these cases it appears that the light-curve parameters can be combined with a flux ratio from a spectrum near maximum brightness to improve the accuracy of SN Ia distances. The best ratios for this, as determined from the BSNIP data, are all near $\mathcal{R}^c (\sim 3750/\sim 4550)$.

This is all somewhat heartening for surveys that will discover and monitor SNe Ia at higher redshifts. Si II $\lambda 4000$, the Mg II and Fe II complexes, and $\mathcal{R}^c (\sim 3750/\sim 4550)$ all involve spectral features which are toward the blue end of the optical range. This is critical for higher- z surveys since, as pointed out in BSNIP II, the red wing of the typical, near-maximum Si II $\lambda 6355$ feature becomes redshifted beyond $\sim 1 \mu\text{m}$ for $z \gtrsim 0.6$. Furthermore, as discussed multiple times in BSNIP II, measuring fluxes and pEWs directly from a spectrum is much easier and less reliant on smoothing models or functional form assumptions than velocities, for example.

To quote the concluding paragraph of Blondin et al. (2011), “Do spectra improve distance measurements of

SN Ia? Yes, but not as much as we had hoped.” We have to agree with the authors of this quote both on the objective part (i.e., spectra *do* improve distance measurements), as well as on the subjective part (i.e., we hoped they would improve things *even more*).

ACKNOWLEDGMENTS

We thank S. J. Bailey, S. Blondin, R. J. Foley, and K. Mandel for useful discussions and comments on earlier drafts of this work, as well as the anonymous referee for comments and suggestions that improved the manuscript. We especially thank J. W. Richards for teaching us statistics; he is a real Ángel. We are grateful to the staff at the Lick and Keck Observatories for their support. Some of the data utilised herein were obtained at the W. M. Keck Observatory, which is operated as a scientific partnership among the California Institute of Technology, the University of California, and the National Aeronautics and Space Administration (NASA); the observatory was made possible by the generous financial support of the W. M. Keck Foundation. We wish to recognise and acknowledge the very significant cultural role and reverence that the summit of Mauna Kea has always had within the indigenous Hawaiian community; we are most fortunate to have the opportunity to conduct observations from this mountain. A.V.F.’s group is supported by the NSF grant AST-0908886, DOE grants DE-FC02-06ER41453 (SciDAC) and DE-FG02-08ER41563, and the TABASGO Foundation. A.V.F. is grateful for the hospitality of the Aspen Center for Physics, where this paper was finalised during the January 2012 program on “The Physics of Astronomical Transients.”

REFERENCES

- Altavilla G., et al., 2009, ApJ, 695, 135
- Amanullah R., et al., 2010, ApJ, 716, 712
- Arsenijevic V., Fabbro S., Mourão A. M., Rica da Silva A. J., 2008, A&A, 492, 535
- Astier P., et al., 2006, A&A, 447, 31
- Bailey S., et al., 2009, A&A, 500, L17
- Benetti S., et al., 2005, ApJ, 623, 1011
- Blondin S., et al., 2006, AJ, 131, 1648
- Blondin S., Mandel K. S., Kirshner R. P., 2011, A&A, 526, A81
- Blondin S., Tonry J. L., 2007, ApJ, 666, 1024
- Bongard S., Baron E., Smadja G., Branch D., Hauschildt P. H., 2006, ApJ, 647, 513
- Cardelli J. A., Clayton G. C., Mathis J. S., 1989, ApJ, 345, 245
- Chornock R., Filippenko A. V., Branch D., Foley R. J., Jha S., Li W., 2006, PASP, 118, 722
- Chotard N., et al., 2011, A&A, 529, L4
- Colgate S. A., McKee C., 1969, ApJ, 157, 623
- Filippenko A. V., et al., 1992a, ApJ, 384, L15
- Filippenko A. V., et al., 1992b, AJ, 104, 1543
- Filippenko A. V., Li W. D., Treffers R. R., Modjaz M., 2001, in Paczyński B., Chen W. P., Lemme C., eds, Small-Telescope Astronomy on Global Scales. The Lick Observatory Supernova Search with the Katzman Auto-

- matic Imaging Telescope. *Astron. Soc. Pac.*, San Francisco, p. 121
- Foley R. J., et al., 2009, *AJ*, 138, 376
- Foley R. J., Filippenko A. V., Jha S. W., 2008, *ApJ*, 686, 117
- Foley R. J., Kasen D., 2011, *ApJ*, 729, 55
- Foley R. J., Sanders N. E., Kirshner R. P., 2011, *ApJ*, 742, 89
- Ganeshalingam M., et al., 2010, *ApJS*, 190, 418
- Garavini G., et al., 2004, *AJ*, 128, 387
- Garavini G., et al., 2007, *A&A*, 470, 411
- Guy J., Astier P., Nobili S., Regnault N., Pain R., 2005, *A&A*, 443, 781
- Guy J., et al., 2007, *A&A*, 466, 11
- Hachinger S., Mazzali P. A., Benetti S., 2006, *MNRAS*, 370, 299
- Hamuy M., et al., 1996, *AJ*, 112, 2408
- Hatano K., Branch D., Deaton J., 1998, *ApJ*, 502, 177
- Hicken M., et al., 2009, *ApJ*, 700, 331
- Hicken M., Wood-Vasey W. M., Blondin S., Challis P., Jha S., Kelly P. L., Rest A., Kirshner R. P., 2009, *ApJ*, 700, 1097
- Hillebrandt W., Niemeyer J. C., 2000, *ARA&A*, 38, 191
- Hoyle F., Fowler W. A., 1960, *ApJ*, 132, 565
- James F., Roos M., 1975, *Computer Physics Communications*, 10, 343
- Jha S., Branch D., Chornock R., Foley R. J., Li W., Swift B. J., Casebeer D., Filippenko A. V., 2006, *AJ*, 132, 189
- Jha S., et al., 2006, *AJ*, 131, 527
- Jha S., Riess A. G., Kirshner R. P., 2007, *ApJ*, 659, 122
- Kaiser N., et al., 2002, in Tyson J. A., Wolff S., eds, *Proceedings of the Society of Photo-Optical Instrumentation Engineers (SPIE) Conference*. Vol. 4836. p. 154
- Kasen D., Plewa T., 2007, *ApJ*, 662, 459
- Kessler R., et al., 2009, *ApJS*, 185, 32
- Kowalski M., et al., 2008, *ApJ*, 686, 749
- Krisciunas K., et al., 2004a, *AJ*, 127, 1664
- Krisciunas K., et al., 2004b, *AJ*, 128, 3034
- Landolt A. U., 1983, *AJ*, 88, 439
- Landolt A. U., 1992, *AJ*, 104, 340
- Law N. M., et al., 2009, *PASP*, 121, 1395
- Leaman J., Li W., Chornock R., Filippenko A. V., 2011, *MNRAS*, 412, 1419
- Leibundgut B., et al., 1993, *AJ*, 105, 301
- Li W., et al., 2000, in Holt S. S., Zhang W. W., eds, *Cosmic Explosions*. American Institute of Physics, New York, p. 103
- Li W., et al., 2001, *PASP*, 113, 1178
- Li W., et al., 2003, *PASP*, 115, 453
- Li W., et al., 2011a, *MNRAS*, 412, 1441
- Li W., et al., 2011b, *MNRAS*, 412, 1473
- Li W., Filippenko A. V., Treffers R. R., Riess A. G., Hu J., Qiu Y., 2001, *ApJ*, 546, 734
- Matheson T., et al., 2008, *AJ*, 135, 1598
- Miller C. J., et al., 2001, *AJ*, 122, 3492
- Miller J. S., Stone R. P. S., 1993, *Lick Obs. Tech. Rep.* 66. Santa Cruz: Lick Obs.
- Nomoto K., Thielemann F.-K., Yokoi K., 1984, *ApJ*, 286, 644
- Nordin J., et al., 2011a, *ApJ*, 734, 42
- Nordin J., et al., 2011b, *A&A*, 526, A119
- Nugent P., Phillips M., Baron E., Branch D., Hauschildt P., 1995, *ApJ*, 455, L147
- O'Donnell J. E., 1994, *ApJ*, 422, 158
- Perlmutter S., et al., 1999, *ApJ*, 517, 565
- Phillips M. M., 1993, *ApJ*, 413, L105
- Phillips M. M., et al., 2007, *PASP*, 119, 360
- Phillips M. M., Wells L. A., Suntzeff N. B., Hamuy M., Leibundgut B., Kirshner R. P., Foltz C. B., 1992, *AJ*, 103, 1632
- Pignata G., et al., 2008, *MNRAS*, 388, 971
- Prieto J. L., Rest A., Suntzeff N. B., 2006, *ApJ*, 647, 501
- Rau A., et al., 2009, *PASP*, 121, 1334
- Riess A. G., et al., 1998, *AJ*, 116, 1009
- Riess A. G., et al., 1999, *AJ*, 117, 707
- Riess A. G., et al., 2007, *ApJ*, 659, 98
- Riess A. G., Press W. H., Kirshner R. P., 1996, *ApJ*, 473, 88
- Savitzky A., Golay M. J. E., 1964, *Analytical Chemistry*, 36, 1627
- Silverman J. M., et al., 2012, *MNRAS*, accepted (arXiv:1202.2128)
- Silverman J. M., Kong J. J., Filippenko A. V., 2012, *MNRAS*, accepted (arXiv:1202.2129)
- Strolger L., et al., 2002, *AJ*, 124, 2905
- Sullivan M., et al., 2011, *ApJ*, 737, 102
- Suzuki N., et al., 2012, *ApJ*, 746, 85
- Valenti S., et al., 2009, *Nature*, 459, 674
- Walker E. S., et al., 2011, *MNRAS*, 410, 1262
- Wang X., et al., 2009, *ApJ*, 699, L139
- Wood-Vasey W. M., et al., 2007, *ApJ*, 666, 694